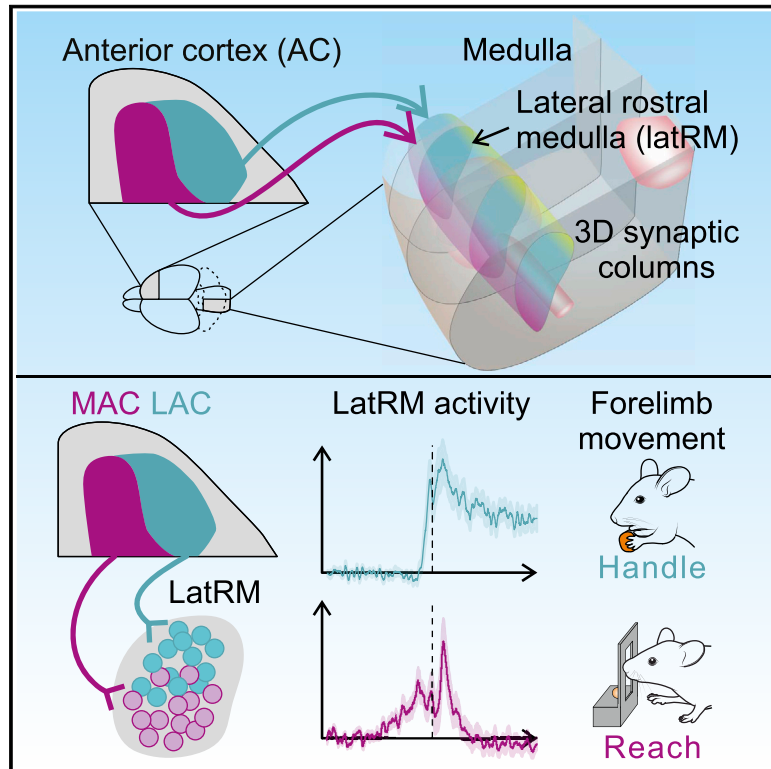


Structural and functional map for forelimb movement phases between cortex and medulla

Graphical abstract



Authors

Wuzhou Yang, Harsh Kanodia,
Silvia Arber

Correspondence

silvia.arber@unibas.ch

In brief

Cortical input dissection to brainstem circuits regulating skilled forelimb movement reveals how anterior cortex territory influences distinct behaviorally tuned brainstem neurons topographically with high anatomical and functional precision.

Highlights

- Brainstem medulla is preferentially innervated by the anterior cortex (AC)
- AC subregions tile forelimb-controlling lateral medulla in 3D synaptic columns
- Function of AC subregions corresponds to forelimb action tuning in downstream medulla
- Parallel cortical pathway topography logic generalizes to other motor centers



Article

Structural and functional map for forelimb movement phases between cortex and medulla

Wuzhou Yang,^{1,2} Harsh Kanodia,^{1,2} and Silvia Arber^{1,2,3,*}

¹Biozentrum, Department of Cell Biology, University of Basel, 4056 Basel, Switzerland

²Friedrich Miescher Institute for Biomedical Research, 4058 Basel, Switzerland

³Lead contact

*Correspondence: silvia.arber@unibas.ch

<https://doi.org/10.1016/j.cell.2022.12.009>

SUMMARY

The cortex influences movement by widespread top-down projections to many nervous system regions. Skilled forelimb movements require brainstem circuitry in the medulla; however, the logic of cortical interactions with these neurons remains unexplored. Here, we reveal a fine-grained anatomical and functional map between anterior cortex (AC) and medulla in mice. Distinct cortical regions generate three-dimensional synaptic columns tiling the lateral medulla, topographically matching the dorso-ventral positions of postsynaptic neurons tuned to distinct forelimb action phases. Although medial AC (MAC) terminates ventrally and connects to forelimb-reaching-tuned neurons and its silencing impairs reaching, lateral AC (LAC) influences dorsally positioned neurons tuned to food handling, and its silencing impairs handling. Cortico-medullary neurons also extend collaterals to other subcortical structures through a segregated channel interaction logic. Our findings reveal a precise alignment between cortical location, its function, and specific forelimb-action-tuned medulla neurons, thereby clarifying interaction principles between these two key structures and beyond.

INTRODUCTION

Motor cortex is the evolutionarily most recent addition to the motor system and influences many regions of the central nervous system.¹ It projects to diverse regions of the motor system processing information relevant to execution and learning of movements. These include well-studied forebrain regions, most notably basal ganglia and thalamus, and structures much closer to motor output, in particular the spinal cord and the brainstem. Uncovering organizational principles of how the motor cortex interacts with different processing stations in the hierarchy of the motor system is of key importance to understand its function.

Although motor cortex is often referred to as a coherent unit, multiple dimensions of anatomical and functional diversity exist. As recent work in the motor cortex revealed, cortical cellular diversity is defined by many parameters including neuronal morphology, molecular, genetic and epigenetic traits, developmental programs, as well as electrophysiological properties.^{2–4} Ultimately, communication and function of cortical neurons is defined by their integration into circuits with specific synaptic input and output patterns. A classical way to probe cortical output potential has been to monitor behavioral patterns elicited by microstimulation of cortical regions. With specificity according to targeted cortical regions, these experiments revealed the generation of movement of different body parts or of goal-directed movements upon longer stimulation trains.^{5–8}

In line with these data and based on recording and perturbation experiments, a cortical map with assignment of functions is beginning to emerge in mice (Figure S1A), including control of forelimbs,^{6,8–12} whiskers,^{13,14} and tongue/jaw.^{15–17} Described roles include learning,^{8,10,18,19} decision-making, and movement preparation¹⁵ as well as precision and adjustments of flexible movements.^{20–22} Strikingly, striatal neurons inherit information from the cortex in precise topography, as shown by anatomical mapping^{23,24} and electrophysiological recordings in behaving mice, with parallel encoding of rich behavioral parameters by cortical and striatal neurons.²⁵ Together, these findings suggest a modular cortical organization with communication specificity to subcortical structures. Therefore, unraveling the principles guiding the organization and function of cortical channels to subcortical neurons central to the orchestration of movement is essential to understand how cortical cell types influence execution and learning of movements. Answering these questions will be particularly informative close to the execution of motor programs, most notably the brainstem and the spinal cord, where movement-relevant information is translated into action.

Skilled forelimb movement is well-suited to address these questions since it requires voluntary control mechanisms to generate precisely timed sequences of muscle activations with different phases, is evolutionarily conserved, and involves cooperation across many nervous system regions including the



cortex.^{26–28} A forelimb behavior evolutionarily conserved across species is reaching for and handling food.²⁸ This behavior consists of timely transport of the hand to the food location through forelimb reaching, food grasping, the retraction of the hand to bring the food close to the mouth, and food manipulation before and during consumption. Recent work in mice provides evidence that neuronal circuits in the most caudal part of the brainstem, i.e., the medulla play an important role in the control of different aspects of skilled forelimb movement including reaching and handling.^{29,30} Experiments in macaque monkeys in which descending cortical axons were cut at mid-brainstem levels, leaving parts of the medulla and all of the spinal cord devoid of cortical input, resulted in profound defects in forelimb movements without affecting posture, locomotion, and other forms of body movement.³¹ Similar defects were also observed upon lateral but not medial descending brainstem pathway lesions.³¹ The combined findings of these lesion experiments and the identification of medullary circuits involved in skilled forelimb movement in mice^{29,30} raise the possibility that cortical input to the lateral medulla might contribute to the control of forelimb movement. Thus, pairing the use of forelimb-based food retrieval as motor behavioral model system, with probing circuit interactions between cortex and forelimb-regulating medullary circuits, represents a perfect opportunity to elucidate principles of functional organization involving cortex.

The cortex communicates with subcortical structures through two classes of projection neurons. Although intratelencephalic (IT) neurons do not extend axons beyond the telencephalon, extratelencephalic (ET) neurons also establish projections to targets outside the telencephalon.^{2,32} In addition, recent work revealed the division of ET neurons into two populations^{2,33}: a medulla-projecting population, which is active during late phases of movement preparation aligned with movement initiation, execution, and termination, and a thalamus-projecting population, which is active mostly during early preparatory time windows.^{33,34} Whether and how the medulla-projecting population interacts with functionally distinct subpopulations in the medulla involved in forelimb movements, possibly breaking down the cortico-medullary functional interaction code, is currently unknown.

To focus on neuronal substrates and interaction principles required to construct skilled forelimb movements in mice, here, we systematically mapped communication topography between cortex and medulla. We found that anterior cortical input is the most prominent source and organized specifically into three-dimensional dorso-ventral (DV) synaptic columns within the lateral medulla. We define a medial cortical region essential for forelimb reaching and preferentially connected to reaching tuned medulla neurons, as well as a lateral cortical region essential for food handling and connected to handling tuned medulla neurons. We also find that the logic of anatomically segregated target innervation by different medulla-projecting cortical neurons extends to other subcortical motor structures by collateralization. Together, these findings reveal the precise anatomical and functional organization between different cortical regions and matched postsynaptic neurons in the caudal brainstem, tuned to different phases of one carefully orchestrated behavior.

RESULTS

Medulla projection neurons reside preferentially in anterior cortex

To determine the location of cortical neurons with projections to the medulla of adult mice, we used adeno-associated viruses (AAVs) with retrograde targeting potential³⁵ expressing a nuclear tag marker protein (rAAV-nTag) (Figure 1A). We targeted the lateral rostral medulla (latRM), a region with established roles in the control of forelimb movement.³⁰ We compared the distribution of latRM cortical projection neurons with that of cortical neurons with projections to the cervical spinal cord (CSC) (C5–C7; Figure 1A). As expected, cortical neurons retrogradely marked from the latRM or CSC were confined to locations with strong bias contralateral to injection sites in cortical areas mostly implicated in sensory-motor functions (Figure 1B; Figure S1A; data not shown). Notably, however, we observed organizational differences along both rostro-caudal and medio-lateral (ML) cortical axes (Figure S1B).

We reconstructed the position of retrogradely labeled contralateral cortical neurons.³⁶ These reconstructions revealed different cortical territories with respect to occupancy by latRM and CSC projection neurons (Figure 1B). First, a caudal cortical domain was occupied predominantly by cervical projection neurons. Second, both types of neurons were found in a rostral antero-medial region and a very lateral caudal domain (barrel cortex [BC]). Third, a cortical region bridging the two intermingled territories, with most neurons laterally adjacent to the anterior-medial cortical domain and extending into the insular cortex (InsC) was almost exclusively occupied by latRM projection neurons. These data suggest that most cortical neurons with access to latRM reside in the anterior cortex (AC). In addition, a segregation into a medial and lateral region occurs within the AC: medial AC (MAC) harbors neurons with projections to medulla and spinal cord, whereas lateral AC (LAC) accesses the medulla but not the spinal cord. Both of these domains are rostral to the classically defined caudal forelimb area (CFA).^{6,9}

To quantify these differences and more clearly delineate the observed domains, we plotted the density of neurons labeled using kernel density estimation (KDE), focusing on sensory-motor cortical regions (Figure 1C). This revealed an anterior and a posterior distribution center for cervical projection neurons (Figure 1C; relative to bregma; anterior center: antero-posterior [AP] +1.8 mm and ML +0.7 mm; posterior center: AP +0.3 mm and ML +1.5 mm), with the caudal center close to the previously described CFA (relative to bregma; AP +0.5 mm and ML +1.5 mm; Figure S1A).^{6,9} In contrast, the peak of the distribution for latRM projection neurons was located laterally within the AC (Figure 1C; relative to bregma; AP +2 mm and ML +1.5 mm), due to the extension of these neurons into the lateral cortex. Most of the latRM-projecting neurons ($84.3\% \pm 3.7\%$; $n = 3$; Figure 1C) were located rostral to +1 mm from bregma, the reported anterior edge of CFA.⁶ Henceforth, we refer to the domain anterior to this boundary as the AC, whereas the cortical domain posterior to it is referred to as the posterior cortex (PC).

Within AC, the vast majority of cervical spinal projection neurons were located medial to +1.5 mm relative to bregma ($94.1\% \pm 1.0\%$; $n = 3$), whereas latRM projection neurons were

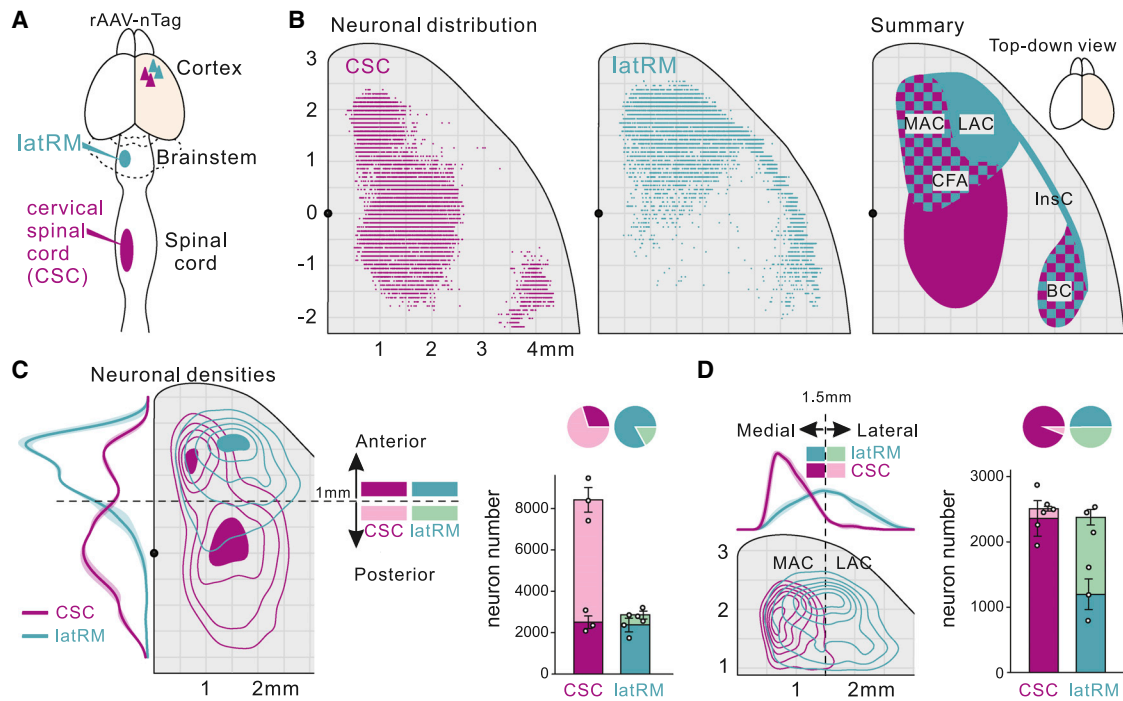


Figure 1. Medulla projection neurons reside preferentially in anterior cortex

(A) Retrograde labeling of cortical neurons from lateral rostral medulla (latRM) and cervical spinal cord (CSC).

(B) Neuronal distribution of cortico-CSC and cortico-latRM neurons (one example mouse each) from top-down cortex view (black marker: bregma). Right: exclusive or overlapping regions in magenta (CSC) and cyan (latRM). MAC, medial anterior cortex; LAC, lateral anterior cortex; CFA, caudal forelimb area; InsC, insular cortex; and BC, barrel cortex.

(C) Density curves (left, mean \pm SEM) show averaged cell density of cortico-CSC and cortico-latRM neurons along the antero-posterior axis. The contour plots show the distribution of respective projection neurons within sensory-motor cortical regions (dashed line: boundary of anterior [AC] and posterior [PC] cortex). Quantification of respective cell proportions and number (mean \pm SEM) in AC and PC for each cortical population (right; $n = 3$ /population).

(D) Left: cell density curves along the medio-lateral axis (top, mean \pm SEM) and contour plot two-dimensional distribution of the averaged cell density for cortico-CSC and cortico-latRM neurons in AC (bottom; dashed line +1.5 mm: boundary between MAC and LAC in our study). Right: quantification of labeled cell proportions and numbers in MAC and LAC for each population ($n = 3$ /population; mean \pm SEM).

See also Figure S1.

distributed about equally medially and laterally to this boundary (medial: $49.7\% \pm 3.3\%$ of AC latRM-projecting neurons; Figure 1D). These results allow for the delineation of a MAC domain, in which neurons reside projecting to CSC and/or latRM and an adjacent LAC domain, in which almost exclusively latRM projection neurons but very sparse spinal cord projection neurons reside (Figure 1D).

We also determined the location of cortical neurons with projections to the lumbar spinal cord, involved in the regulation of hindlimb movement. In agreement with previous work,³⁷ we found that these neurons were located very caudally within motor cortical territory (Figure S1C; center relative to bregma at AP -1 mm and ML $+1.2$ mm), demonstrating a lack of overlap in cortical location between latRM and lumbar spinal cord projection neurons.

Together, our results demonstrate that cortical regions have differential access to latRM and the spinal cord. Cortical access to the latRM occurs preferentially from AC. Within this domain, cortical neurons with selective access to latRM but not to the spinal cord define the LAC, whereas MAC harbors both populations of cortical neurons (Figures 1D and S1). These lateral anatomical

characteristics extend into the InsC, which also does not contain spinal projection neurons. The delineation of these cortical domains based on retrograde tracing raises the question of whether a more fine-grained spatial organization might exist for the communication between cortex and medulla.

Cortex provides topographically organized synaptic input to latRM

We next carried out systematic injections of AAVs into the cortex of adult wild-type mice ($n = 30$), using our retrograde map as a guide to define cortical areas of interest. We injected a cocktail of Cre-conditional AAVs to express different marker proteins targeted to the cytosol (CytTag), the synapse (SynTag), and the nucleus (nTag) of infected neurons together with an AAV-Cre to induce their expression (Figure 2A). Through visualizing the cytosolic tag (CytTag) in the medulla, we found that, as expected, descending cortical axons extended ipsilaterally to injection, and most axon collaterals emerging in the medulla crossed the midline to shoot toward the contralateral side (data not shown). We restricted further analysis to the medulla contralateral to cortical injection.

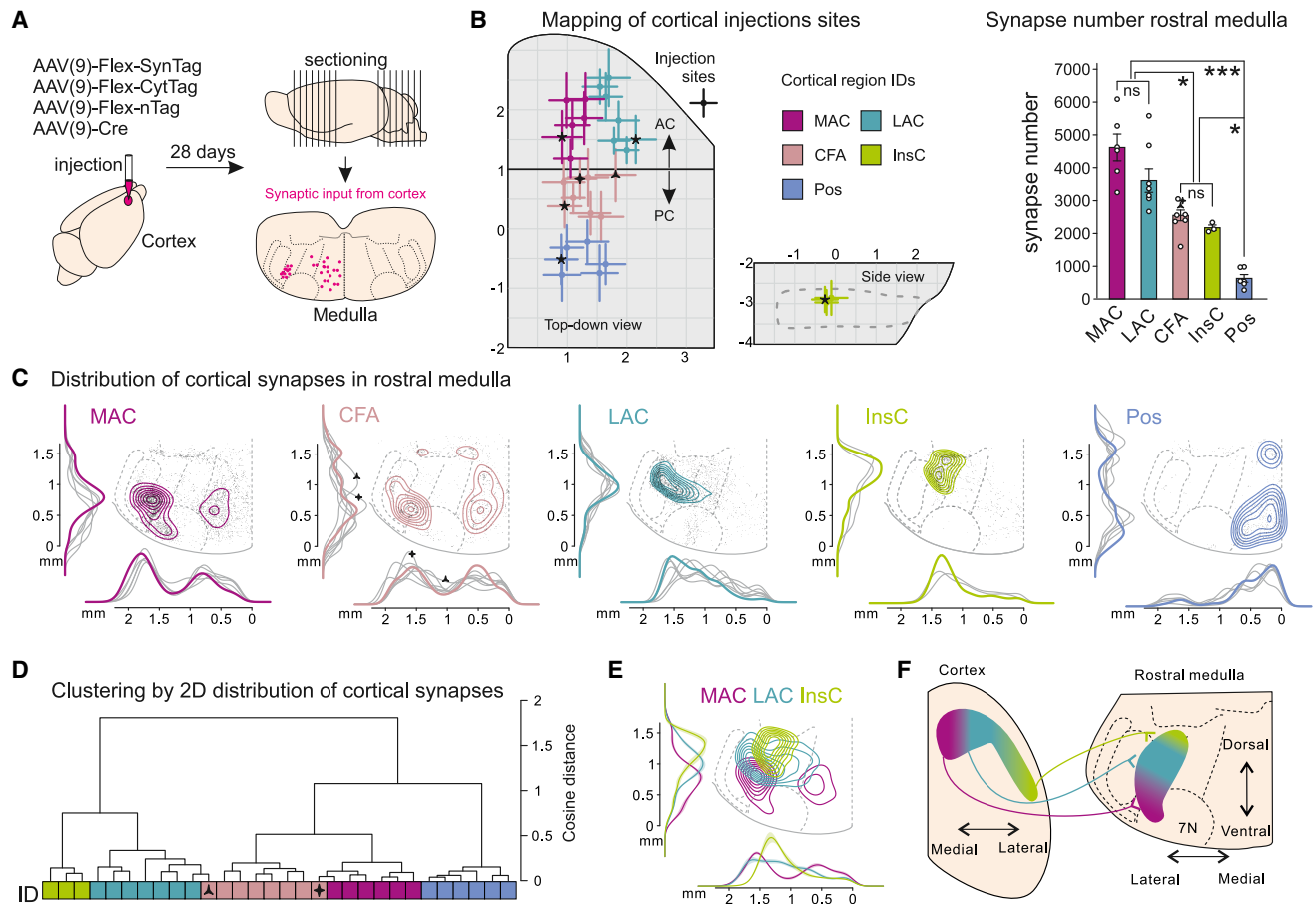


Figure 2. Cortex provides topographically organized synaptic input to latRM

(A) Strategy for cortical injections to map cortico-medullary projections.

(B) Left: injection sites color-coded by cortical regions. Stars indicate the injection sites of examples shown in (C). Right: bar plot of synapse number in rostral medulla according to different cortical injection site groups (mean \pm SEM). Triangles and diamonds indicate injection sites marked in (C) and (D) residing at the border between AC and PC. MAC, $n = 6$; LAC, $n = 7$; CFA, $n = 8$; InsC, $n = 3$; Pos, $n = 6$. * $p < 0.05$; *** $p < 0.001$; ns, not significant.

(C) Distribution of cortical synaptic puncta and density in rostral medulla including dorso-ventral and medio-lateral densities from representative injections (colored curves: example density distribution from each cortical region for injection sites indicated in B with stars; gray curves: dorso-ventral and medio-lateral densities from all other injection sites).

(D) Clustering of injection sites based on the spatial distribution patterns of cortical synapses in rostral medulla from all injection sites.

(E) Averaged synaptic densities of 2D distribution including dorso-ventral and medio-lateral densities (mean \pm SEM) from MAC, LAC, and InsC in rostral medulla (MAC, $n = 6$; LAC, $n = 7$; InsC, $n = 3$).

(F) Summary of anatomical organization between cortex and latRM.

See also [Figure S2](#).

We first determined the distribution of synaptic input to the medulla from the different cortical injection sites, based on SynTag immunofluorescence ([Figure S2A](#)). We compared synapse numbers across all cortical injection sites ([Figures 2B and S2B](#)) focusing on the facial motor nucleus (7N) level (bregma -6 mm; [Figure S2C](#)). We found that AC including MAC and LAC contributed the highest number of synaptic puncta ([Figure 2B](#)). Lower numbers were contributed by CFA and InsC, with the sparsest synaptic contribution from domains posterior to CFA (here referred to as Pos) ([Figure 2B](#)). These cortical synaptic abundance differences were observed also at two more caudal medullary levels up to the hypoglossal motor nucleus (12N) level ([Figures S2C–S2E](#)). Together, these findings

demonstrate that AC regions produce anatomically more pronounced synaptic input to the medulla than PC regions.

To determine which regions of the medulla are the main targets for synaptic input from the cortex, we analyzed data for their synaptic distribution at the 7N level. We pooled injection sites according to the regions defined by retrograde infection (MAC, LAC, CFA, InsC, and Pos) and mapped the 2D synaptic densities along ML and DV axes ([Figure 2C](#)). We found that synaptic distributions from MAC and CFA exhibited a bimodal distribution along the ML axis, although MAC showed more pronounced synaptic terminations in the latRM. In contrast, synaptic output from LAC and InsC injections were biased laterally. Synaptic output from Pos injection sites, although generally sparse as described above,

avoided latRM territory and instead was directed to the medially located gigantocellular nucleus region (Gi; Figure 2C). We confirmed these findings by calculating a laterality index to estimate the lateral bias of the synaptic distribution, demonstrating that indeed the four cortical regions with the most abundant synaptic contribution to the 7N level (MAC, LAC, CFA, and InsC) also exhibited higher values in the laterality index (Figure S2F).

In addition to the ML organization, we also observed a topographic organization of synaptic input along the DV axis according to the source of its cortical origin (Figure 2C). MAC- and CFA-derived synaptic input was directed to the most ventral region of the latRM, followed by a region with highest input from LAC and abutted by input from InsC most dorsally along the latRM axis (Figures 2C and 2E). These data demonstrate that the latRM is the main cortical synaptic target at the 7N level. Moreover, cortical input to the latRM is topographically arranged, with synaptic input from InsC, LAC, and MAC tiling the latRM along its DV axis (Figures 2C and 2E).

The synaptic distribution patterns for the injections within each cortical domain (MAC, LAC, CFA, InsC, and Pos) were markedly more correlated and similar to the other injections within the group as demonstrated by a hierarchical clustering dendrogram (Figure 2D). We found that different cortical injection sites clustered together, indicating that they share similar synaptic distribution patterns. There were two injection sites that did not obey the clustering hierarchy, which were however along the rostral edge of the CFA boundary invading MAC or LAC territory, respectively, explaining the seeming discrepancy (Figures 2B and 2D). Together, these findings demonstrate that the majority of 7N medullary level cortical synapses are directed toward the lateral medulla and derived from AC including MAC, LAC, and InsC. These synapses tile the lateral medulla along the DV axis in a fine-grained map (Figure 2F).

Cortical input to medulla is organized in 3D rostro-caudal columns

To determine whether and how this revealed spatial organization might generalize to the three-dimensional extent of the medulla, we next applied the same analysis to intermediate and caudal medulla levels (Figure 3A; Figure S2C). We chose the 12N level as caudal medulla (bregma -7.32 mm) and a level midway between these two positions as intermediate medulla (bregma -6.64 mm)³⁶ (Figure S2C). We found that the highest density of synaptic terminals derived from MAC was confined to ventral territory at both intermediate and caudal medulla levels (Figures 3A and 3B). In contrast, analysis of synaptic output from LAC revealed a termination zone dorsally adjacent to terminals from MAC, and analogous analysis of InsC synaptic output resulted in the most dorsal termination zone in sequence (Figures 3A and 3B). These findings were confirmed by analyzing the peak of highest synaptic density along the DV axis across the three rostro-caudal levels (Figure 3C).

We constructed a spatial similarity matrix of the different injection sites in the cortex combining information on the synaptic organization from all three medullary levels to obtain the 3D synaptic distribution (Figure 3D). This analysis showed that all injection sites fall into the groups assigned by retrograde tracing, displaying higher correlation of synaptic distribution patterns within

the group than across groups. Moreover, LAC and InsC as well as MAC and CFA are more correlated to each other, whereas Pos was the least correlated with all other groups (Figure 3D). We conclude that the synaptic output of MAC, LAC, and InsC is directed to rostro-caudally arranged columns along the medullary DV axis (Figure 3E), extending the logic of cortical synaptic organization within the medulla to a 3D configuration.

Individual cortical neurons form collaterals along the rostro-caudal medulla

We next asked whether these 3D cortical axon terminal columns are the product of individual cortical neurons each giving rise to several collateral branches and associated synapses along the rostro-caudal axis, or alternatively, whether they represent a composite of arborizations each exhibiting only one restricted termination zone along the rostro-caudal axis. We turned to the MouseLight project from the Janelia Research Campus,⁴ where axonal arborization of individual neurons was reconstructed. We searched the library for cortical neurons within the here-analyzed cortical territory with axons ramifications in the medulla and found MAC ($n = 7$) and LAC ($n = 6$) neurons (Figures 4A and 4B; Figure S3). In agreement with our own overall tracing experiments (Figure 3E), we observed a differential DV synaptic distribution of axon terminals within the lateral medulla when separately grouping MAC and LAC neurons together (Figure 4C).

Analysis along the rostro-caudal dimension showed that within the medulla, we observed quite some variability at the level of individual neurons with respect to the extent of axonal collateralization, arborization, and presumptive associated synaptic boutons generated (Figure S3). However, collaterals from the parent axon generally branched off at multiple rostro-caudal levels, exhibiting proliferative axonal growth within the lateral medulla, with a preference for the side contralateral to cortical cell body location (Figures 4D and 4E; Figure S3). We visualized and quantified the distribution of axon terminals, plotted their density along the rostro-caudal axis in the medulla and observed that neurons generally had axon terminals distributed at multiple levels in the AP dimension (Figure 4E). This analysis demonstrates that although the sum of reconstructed axon terminals of individual cortical neurons never filled the entire rostro-caudal extent, individual MAC and LAC neurons generally synaptically contact the lateral medulla at multiple locations within the overall rostro-caudal medullary column. Together, our analysis demonstrates that cortical input to the medulla even at the single neuron level does not represent a simple point-to-point communication but rather follows a signaling mode with interactions in a three-dimensional volume at multiple locations of the medulla in a top-down manner.

Selective roles for MAC vs. LAC in reaching vs. handling

Given the striking difference in anatomical input organization from MAC and LAC to forelimb-regulating regions in the medulla, respectively, we next set out to probe the function of these two cortical domains in forelimb control. We trained mice to perform a pellet reaching and food manipulation task, which we had previously shown to recruit specific latRM neurons in a task- and behavioral-phase-dependent manner.³⁰ We analyzed its two main phases, i.e., the food retrieval phase

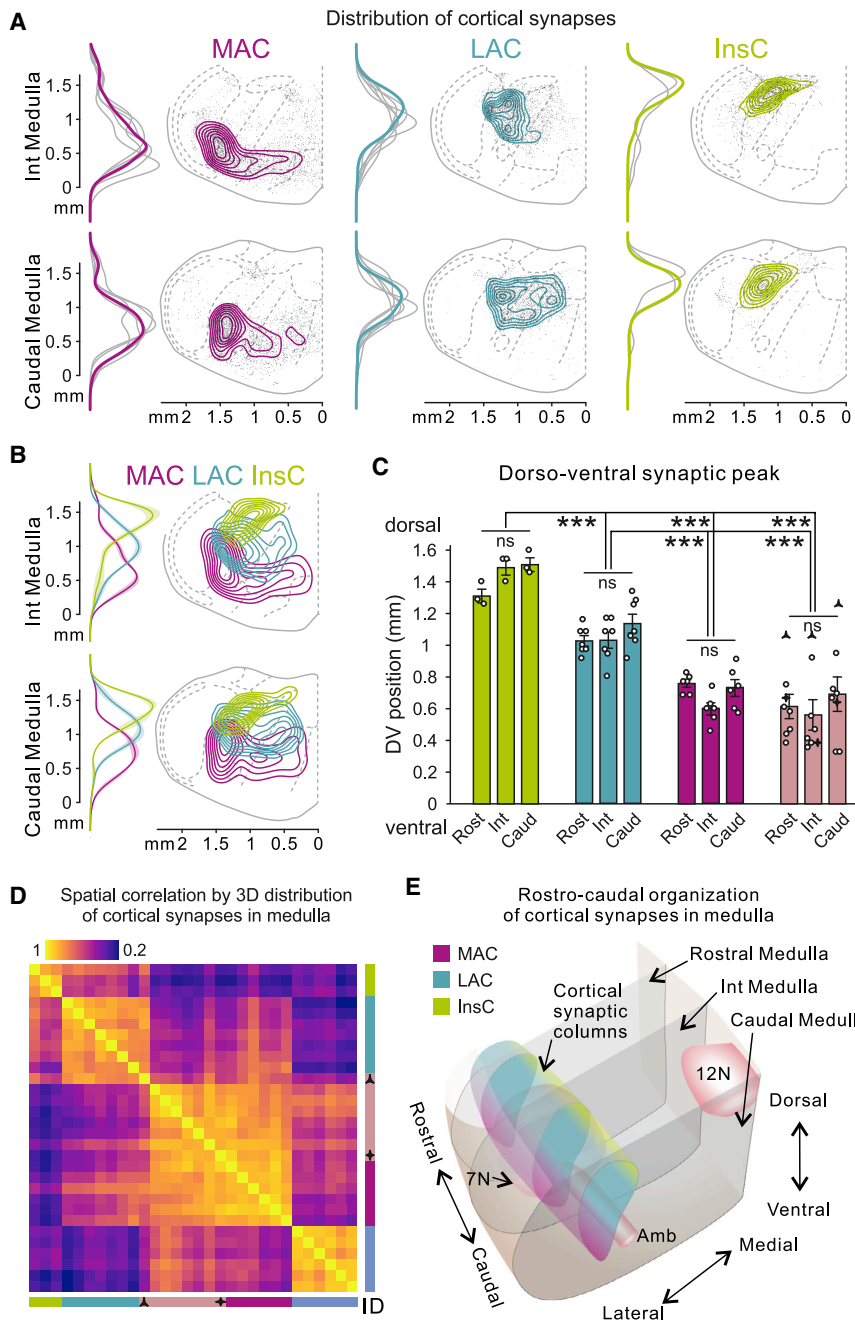


Figure 3. Cortical input to medulla is organized in 3D rostro-caudal columns

(A) Distribution of cortical synaptic puncta and density at intermediate and caudal medulla levels from representative injections in MAC, LAC, and InsC indicated in Figure 2B with stars, including dorso-ventral density distributions (gray curves: density distributions from other injection sites). (B) 2D distributions of averaged synaptic densities and average density along the dorso-ventral axis (mean \pm SEM) from MAC, LAC, and InsC (MAC, $n = 6$; LAC, $n = 7$; InsC, $n = 3$). (C) Dorso-ventral position of peak synaptic distribution from MAC, LAC, InsC, and CFA injections at the three medullary levels (mean \pm SEM). ** $p < 0.01$; *** $p < 0.001$; ns, not significant. (D) Spatial correlation analysis of synaptic distribution patterns at analyzed medullary levels. (E) 3D scheme of cortical input to the rostro-caudal medullary axis.

food pellet (Video S1). Quantitative analysis from high speed videos by tracking reaching trajectories using DeepLabCut (DLC)³⁸ demonstrated a highly significant decrease in the number of executed reaches per minute and the maximum extension of the forelimb toward the pellet in MAC-silenced mice compared with either LAC-silenced or control mice (Figures 5C and 5D). Moreover, although reaching speed could not be quantified from MAC-silenced mice owing to their inability to reach, LAC-silenced mice were not different from control mice in this parameter (Figure 5C).

A strikingly different result was obtained when we analyzed the second behavioral phase of the assay, which consisted of handling/manipulating food and consuming it (Figure 5E; Video S2). LAC silencing led to deficits in food manipulation, due to which the mice consumed food directly from the ground for long periods of time, without engaging their forelimbs to manipulate it, whereas MAC-silenced or control mice used almost exclusively their forelimbs to eat

comprised a directed forelimb reaching and retrieval action, as well as the consummatory phase during which mice handle the food pellet while eating.

We tested the effect of acute silencing by cortical muscimol injections into either MAC or LAC on behavioral performance (Figure 5A). Mice were trained to retrieve a food pellet (Figure 5B). During this first behavioral phase of the assay, silencing of MAC, but not LAC had a dramatic effect on reaching (Figures 5C and 5D), essentially leading to the complete inability to extend the forelimb through the slit toward the

(Figure 5E). Moreover, in the phases when LAC-silenced mice used the forelimbs to hold food, we observed they frequently dropped the food pellet, a property neither observed in MAC-silenced nor control mice (Figure 5E). To determine why LAC-silenced mice resorted to eat without forelimb food manipulation, we carefully analyzed the episodes during which they hold food pellets in their hands and compared them with corresponding episodes in MAC-silenced or control mice (Figures 5F and 5G; Video S2). We found that during food pellet manipulation, mice exhibit stereotyped regrip movements (regrips) with their

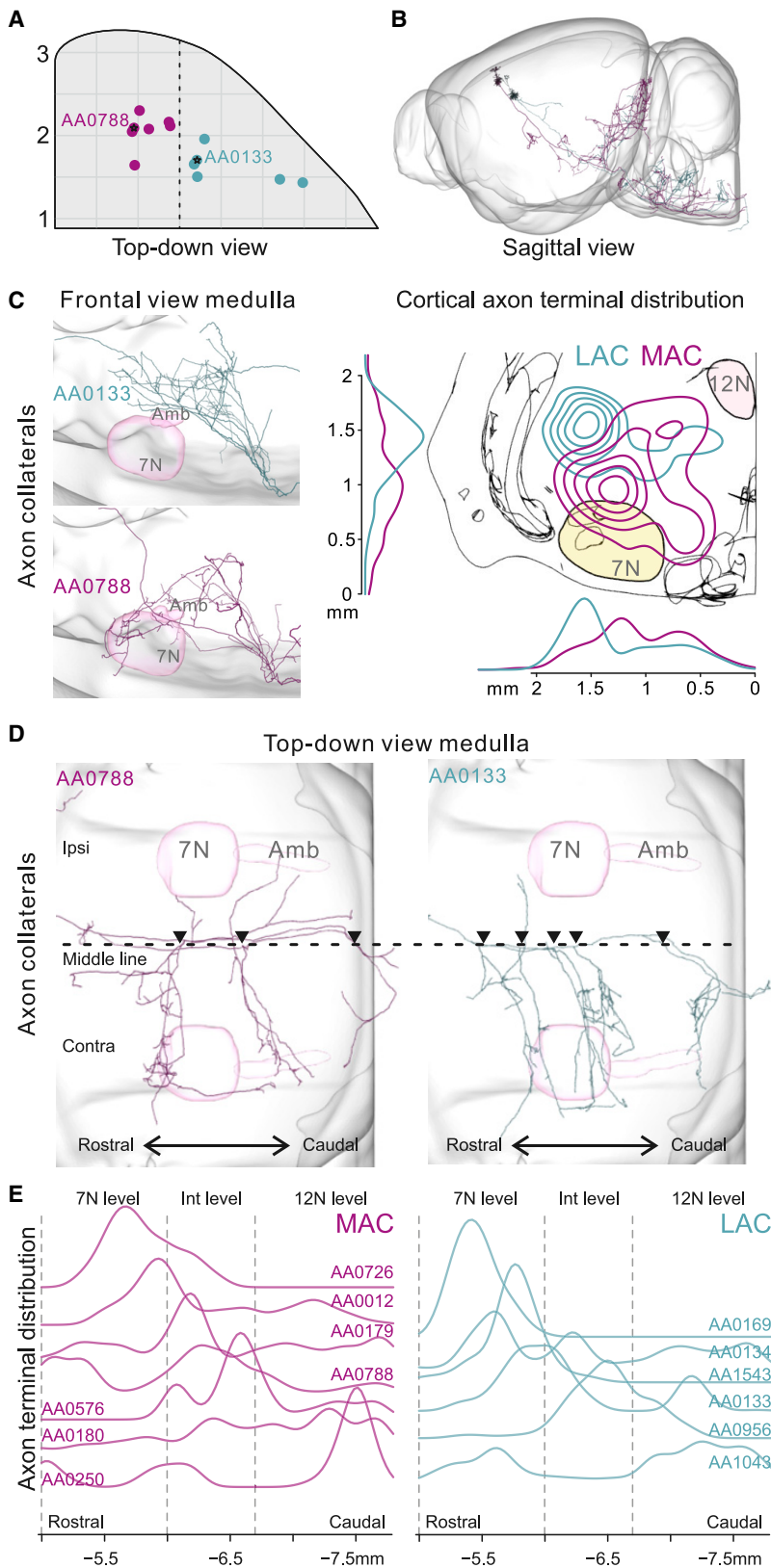


Figure 4. Individual cortical neurons form collaterals along the rostro-caudal medulla

(A) Scheme of soma location for the MouseLight database neurons in MAC and LAC (MAC: n = 7; LAC: n = 6; mirroring to right hemisphere; stars: neurons shown in B–D).

(B) Representative MAC and LAC neuron in the sagittal view in 3D model.

(C) Left: frontal view of axons in the medulla from the two example neurons. Right: 2D, dorso-ventral and medio-lateral axon terminal distribution in the medulla shown in coronal view from all neurons in (A).

(D) Top-down view of axons in the medulla from the two examples neurons (triangles: axonal collaterals exiting from parent main axon at multiple rostro-caudal levels).

(E) Rostro-caudal axonal terminal distribution of single cortical neurons in medulla.

See also Figure S3.

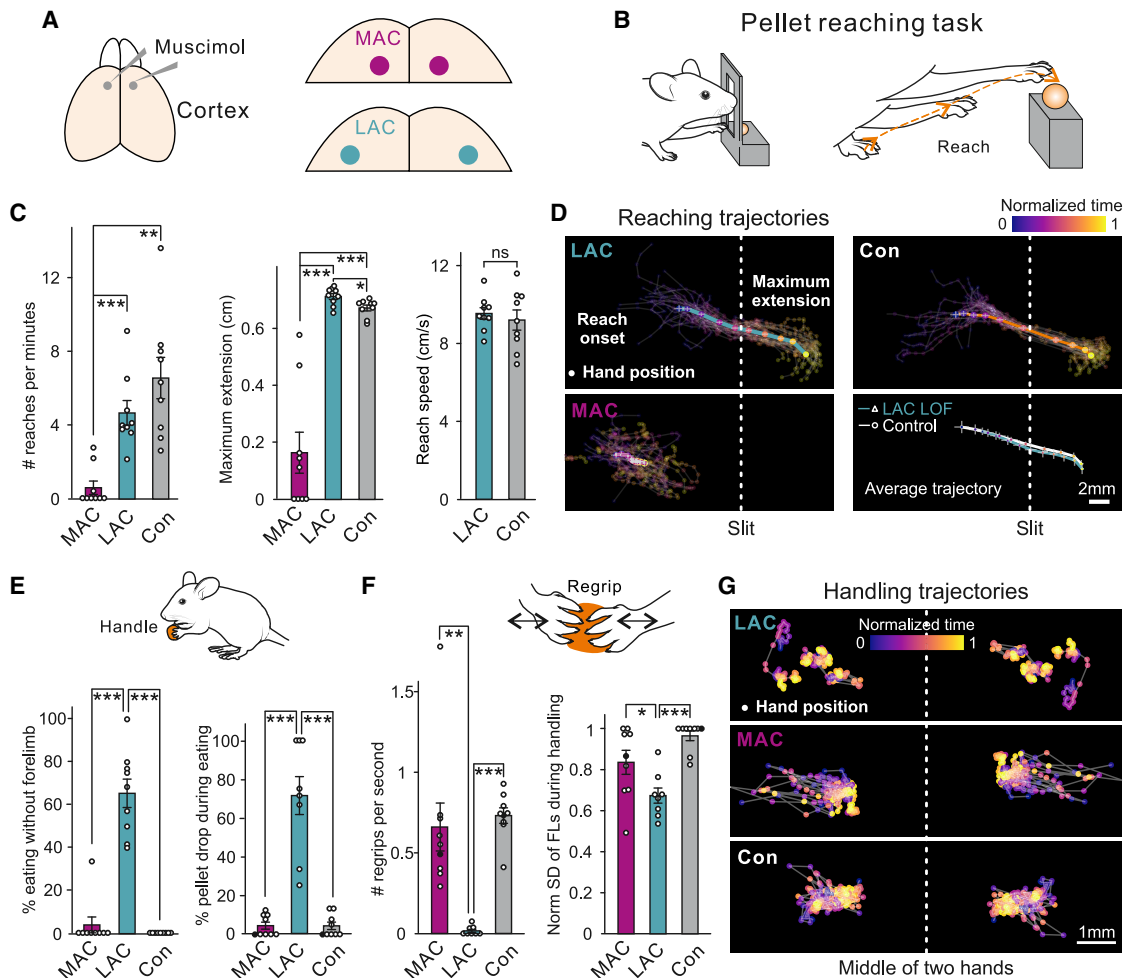


Figure 5. Selective roles for MAC vs. LAC in reaching vs. handling

(A) Strategy for silencing of identified cortical domains using bilateral muscimol injections into MAC or LAC.

(B) Pellet reaching task illustrating the elaboration of the reaching trajectory.

(C) Quantification of the number of reaches per minute (left), maximum extension of the forelimb from the slit (middle), and speed of reaching (right) with silencing of MAC and LAC compared with control (mean \pm SEM, $n = 9$ mice).

(D) Reaching trajectories with MAC or LAC silencing compared with control (top and lower left: trajectories from one example mouse; colored curves: averaged trajectories from all gray curves per condition; LAC, 30 trials; MAC, 22 trials; Con, 31 trials; lower right: average trajectory comparison for LAC silencing and control conditions; $n = 9$ mice; dots colored by normalized time denote hand position at normalized time points during reaching; averaged hand positions shown as mean \pm SEM).

(E) LAC silencing impairs food handling (scheme). Bar plots showing the percentage of food handling bouts without forelimb usage (left, mean \pm SEM, $n = 9$ mice) and percentage of handling bouts terminating with food pellet dropping (right, mean \pm SEM, $n = 8$ mice). One mouse (black dots in MAC and Con) used exclusively the mouth to consume food with LAC silencing (see also F).

(F) Quantification of number of regrips (scheme) per second during the handling bout (left) and normalized standard deviation of the limb mid-point centered trajectories (right) across experimental conditions ($n = 8$ mice).

(G) Limb mid-point centered forelimb trajectories during food handling from one example mouse across conditions (7 handling bouts per mouse; dots colored by normalized time denote hand position at normalized handling time points).

* $p < 0.05$; ** $p < 0.01$; *** $p < 0.001$; ns, not significant.

See also Videos S1 and S2.

distal forelimbs and digits. These regrips were observed at comparable frequency in MAC-silenced and control mice but were essentially absent in LAC-silenced mice (Figure 5F). The loss of regrips in LAC-silenced mice was also evident from the decrease in the movement of the distal forelimbs during handling (Figure 5F).

Together, these results demonstrate that MAC and LAC are essential for mice to proficiently perform the food pellet reaching and handling task, but strikingly, they are needed for distinct behavioral phases. Although MAC is required for the reaching phase, in agreement with previous optogenetic silencing experiments,³⁹ LAC is essential for handling and manipulation phases

recruiting distal forelimb muscles, but completely dispensable for the reaching phase.

Cortico-medullary synaptic organization extends into postsynaptic medulla

The strikingly different roles of MAC and LAC in controlling reaching and handling raised the question of which neurons in the latRM are the targets for these different cortical inputs. To assess the identity of medullary neurons in relation to cortical input sources, we first determined the location of latRM neurons postsynaptic to different cortical regions. We took advantage of an AAV serotype exhibiting anterograde transfer potential for recombinase expressing cargos.^{40,41} We injected a cocktail of AAVs expressing different recombinases (AAV(1)-Cre and AAV(1)-FLP) into two different cortical regions (MAC and LAC, or LAC and InsC, respectively) together with a cocktail of corresponding reporter constructs (AAV(9)-flex-CytTag1 and AAV(9)-frt-CytTag2) into latRM contralateral to cortical injections (Figures S4A and S4B). Postsynaptic mapping of latRM neurons from MAC and LAC revealed an overall more ventral position for MAC-recipient medulla neurons, whereas analogous experiments from LAC and InsC resulted in InsC-recipient neurons in a more dorsal position than LAC counterparts (Figure S4C). Quantification of marked medulla neurons including all datasets allowed to determine the distribution of these neurons in the latRM (Figure S4D; Video S3). We found that MAC-input neurons were located most ventrally, followed by LAC- and InsC-input neurons with highest densities in progressively more dorsal positions (Figure S4D; Video S3). Strikingly, the overall neuronal distribution patterns in latRM were reminiscent of the synaptic input patterns from the corresponding cortical regions (Figure 2C). Together, these findings demonstrate that the communication from different cortical regions to the medulla is highly organized and that postsynaptic recipient neurons in the latRM faithfully follow the distribution of cortical synaptic input.

Functional tuning of medulla neurons aligned with specific cortical input

To determine whether individual latRM neurons receive preferential functional cortical input from MAC or LAC and how this relates to their behavioral tuning during skilled forelimb movement, we next used *in vivo* electrophysiological recordings in latRM combined with cortical stimulation by optogenetics (Figure 6A). We delivered short pulses (50 ms) of light to either stimulate MAC or LAC neurons while recording activity from single latRM units. We identified 21 MAC- and 15 LAC-modulated latRM neurons, defined by a short latency firing rate increase in response to cortical stimulation (significant increase at latencies ≤ 20 ms; Figures S5A–S5D).

We next determined the tuning properties of these cortex-modulated latRM neurons to the different behavioral phases of the pellet reaching and handling task (Figure 6B). We recorded from a total of 726 neurons in latRM (Figure S5). Consistent with a previous study,³⁰ neurons in latRM (54.1%; 393/726) were positively modulated during different forelimb task phases (Figures S5 and S6), whereas 13.4% (97/726) of the neurons were only negatively modulated (Figure S7) and 32.5% (236/726) were not modulated. Focusing specifically on the pop-

ulations positively modulated by MAC and LAC, we found that MAC-modulated latRM neurons exhibited strikingly different behavioral tuning properties LAC-modulated ones (Figures 6C–6E). Averaged population activity showed that the MAC-modulated population exhibited an increase in firing rate preceding the onset of forelimb reaching, whereas the LAC-modulated population sharply increased firing rate only thereafter (Figure 6D, left). In contrast, the LAC-modulated population exhibited increasing firing preceding food handling onset, whereas the MAC-modulated population sharply downregulated its activity around this behavioral transition with the onset of handling (Figure 6D, right). This was also reflected in the activity of the single latRM neurons giving rise to the population activity. Although LAC-modulated latRM neurons almost exclusively showed increases in activity corresponding to the onset of handling and manipulation of the food pellet, individual MAC-modulated neurons showed transient increase in activity that over all the analyzed neurons tiled the behavior space of the reaching task preceding the handling of the food pellet (Figures 6D and 6E). Together, these experiments provide striking functional evidence for highly selective interactions between cortex and latRM neurons with respect to different forelimb movement phases. Although LAC input is directed almost exclusively to latRM neurons tuned to handling, MAC input is preferentially directed to latRM neurons active during phases preceding food manipulation (pre-reaching, reaching, and retraction).

Topography of cortico-medulla neurons extends to other subcortical structures

The striking anatomical and functional output organization of medulla-projecting cortical neurons raises the question of whether and how these populations collateralize to subcortical motor system targets other than the medulla. This is interesting in light of recent observations that cortical output neurons stratify into two populations based on whether they innervate thalamic targets³³ and that cortical neurons with projections to the CSC preferentially target striatal D1-receptor expressing neurons.⁴² We analyzed the collateralization patterns of latRM-projecting MAC, LAC, and InsC neurons to several subcortical regions. As subcortical structures within the general motor cortical output pathway with known overall cortical input we selected (1) the superior colliculus (SuC), an important multi-sensory integration center in the midbrain, (2) the striatum, the input layer to basal ganglia circuitry, (3) the subthalamic nucleus (STN), the excitatory intermediate target within the indirect basal ganglia pathway and target for the hyperdirect pathway from the cortex, and (4) substantia nigra (SN), the biggest basal ganglia output nucleus in rodents.

We injected retrograde AAV expressing Cre recombinase into latRM to selectively induce CytTag and SynTag expression specifically in medulla-projecting cortical populations (MAC, LAC, and InsC) (Figure 7A). Consistent with single neuronal tracing data (Figure 4), axon collaterals from marked cortico-medulla neurons targeted exclusively territory ipsilateral to cortical injection subcortically rostral to the medulla but exhibited a biased targeting of axons to regions contralateral to injection within the medulla (Figure 7A; data not shown). Therefore, we analyzed the synaptic output patterns of MAC-, LAC-, or InsC-latRM

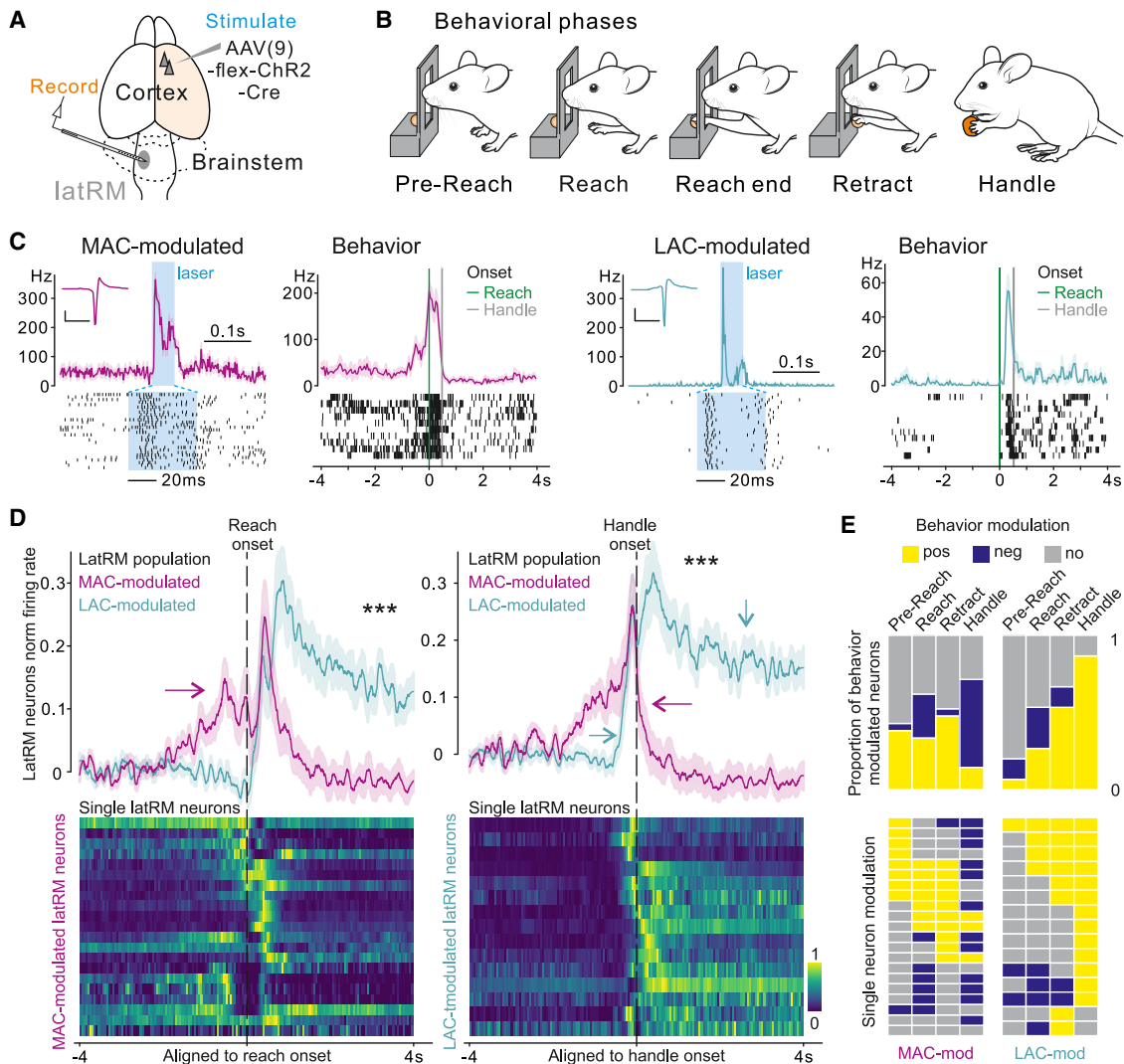


Figure 6. Functional tuning of medulla neurons aligned with specific cortical input

(A) Strategy to identify the effect of cortical input to latRM neurons using cortical neuron stimulation while recording in the latRM.

(B) Scheme of different phases of the reaching and handling task annotated.

(C) Effect of cortical stimulation on latRM neurons and activity of the same neuron during the task. MAC-modulated (left) and LAC-modulated (right) latRM example neurons responding at short latency to cortical stimulation depicting average firing rate (top), raster plot (bottom), and average waveforms with scale bars denoting 100 μ V (vertical) and 1 ms (horizontal).

(D) Top: population level activity of MAC-modulated (magenta) and LAC-modulated (cyan) latRM neurons with the average normalized firing rate of the respective populations aligned to reaching onset (left) or handling onset (right). Bottom: baseline subtracted and normalized firing of single neurons for MAC-modulated (left, aligned to reach onset) and LAC-modulated (right, aligned to handle onset) populations. *** $p < 0.001$; MAC-modulated neurons, $n = 21$ from 5 mice; LAC-modulated neurons, $n = 15$ from 8 mice.

(E) Top: proportion of MAC- or LAC-modulated neurons modulated during different behaviors (B). Bottom: modulation of each neuron shown in (D) (yellow: positive modulation; blue: negative modulation; gray: no modulation).

See also [Figures S5](#), [S6](#), and [S7](#).

projection neurons to the ipsilateral striatum, STN, SN, and SuC ([Figure 7A](#)). The quantification of synaptic distribution allowed us to score the similarity of synaptic patterns in target structures either considering all of these subcortical target structures ([Figure 7B](#)) or by individual target structures ([Figures 7C–7F](#)). We found that latRM projection neurons located in MAC also establish collaterals and synaptic input to a restricted domain of the motor layers of the SuC sparing its most lateral corner of inner-

vation, an intermediate part of the lateral striatum, the ventral domain of the STN as well as to a ventral intermediate region of the SN pars reticulata (SNr; [Figures 7C–7F](#); [Figure S8](#)). In contrast, LAC neurons with axons to the medulla also terminated in the lateral most corner of the SuC, a ventral part of the lateral striatum, the dorsal domain of the STN, and in a lateral dorsal domain of the SNr ([Figures 7C–7F](#); [Figure S8](#)). Finally, we analyzed InsC neurons with collaterals to the medulla and found

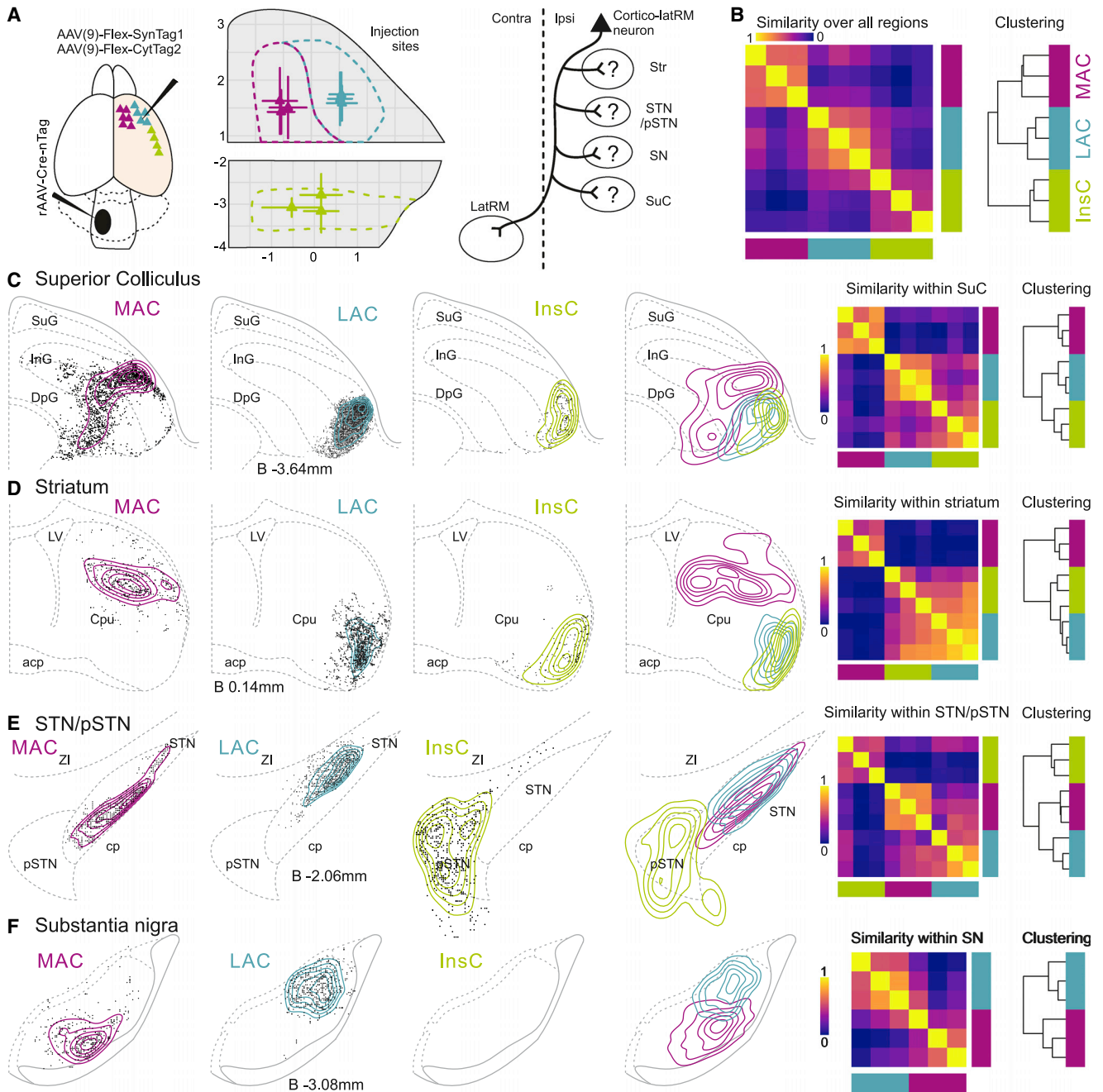


Figure 7. Topography of cortico-medulla neurons extends to other subcortical structures

(A) Anterograde tracing of cortico-medullary neurons (left), cortical injection sites (middle), and scheme of collateral arborization patterns (right) (MAC, n = 3; LAC, n = 3; InsC, n = 3). Abbreviations are as follows: Str, striatum; STN/pSTN, subthalamic nucleus/parathalamic nucleus; SN, substantia nigra; and SuC, superior colliculus.

(B) Spatial correlation analysis (left) and clustering (right) of synaptic distribution patterns in subcortical regions across levels shown in (C)–(F) and Figure S8. (C)–(F) Top: representative 2D reconstruction of synaptic puncta and density distributions in superior colliculus (C), striatum (D), STN/pSTN (E), and substantia nigra (F) from 3 mice with labeled cortico-medullary neurons in MAC, LAC, and InsC, respectively. Middle: 2D reconstruction of averaged synaptic density distribution overlaid. Right: spatial correlation analysis and clustering of synaptic distribution patterns at the subcortical regions from all levels analyzed in Figures 7 and S8.

See also Figure S8 and Video S4.

these to be distinct in the elaboration of collaterals to other subcortical structures from MAC and LAC. Specifically, although there was some overlap between LAC and InsC output in the SuC, these were still distinct enough to segregate the cortical domains in the computational similarity analysis. Moreover, LAC and InsC output was strikingly segregated within the STN region, where InsC input targeted the adjacent para-STN (pSTN) region rather than the STN proper, and no significant input was observed for InsC to the SNr (Figures 7C–7F; Figure S8). We also evaluated axonal terminations of cortico-medullary projection neurons in the thalamus, which in agreement with previous work³³ did not represent a major target structure for either of these three populations (data not shown). Finally, combined analysis of axon terminals in the striatum and SuC from single MAC and LAC neurons of the MouseLight database also showed spatial segregation (Video S4).

Together, these findings demonstrate that the here characterized different populations of cortico-medulla projection neurons not only follow a highly granular logic for how their synaptic input targets medullary neurons. Strikingly, at the same time, these neurons establish collaterals to several other subcortical regions with patterns of high spatial organization and distinction. Our findings thus generalize the logic of how these neurons interact within the motor system beyond the medulla.

DISCUSSION

Understanding how the cortex influences subcortical movement centers requires the identification of interaction principles between cortex and subcortical structures. The medulla is a major cortical target in the motor output system³³ involved in key aspects of forelimb movement control,^{29,30} defining the focus of this study. Here, we demonstrate that the cortex elaborates highly specific channels targeting precisely arranged 3D columns in forelimb-movement controlling regions in the medulla, preferentially interacting with neurons tuned to specific forelimb action phases. We demonstrate that these channels are aligned with the functional requirement of respective cortical regions in reaching and handling phases of forelimb movement. Our findings shed light on how large cortical territory topographically influences behaviorally tuned circuits in the medulla in a top-down manner with channels of high functional precision. We discuss the organizational logic of these signaling strategies, the implications of our findings for understanding motor system function and how these findings generalize to other motor centers.

Organization of cortical input to medulla and spinal cord for forelimb control

Cortico-spinal neurons have been a main focus of studies on neuronal control of forelimb movement, demonstrating differential access to spinal segments, axonal termination zones, or connectivity to spinal neurons.^{1,8,42–45} Our work uncovers a striking organization for synaptic interactions between cortex and medulla and identifies LAC as a cortical domain without access to the spinal cord but strong interactions with the medulla. Interestingly, high-density synaptic input to the medulla is preferentially derived from anterior cortical territory and targets regions of the

medulla implicated in forelimb control,^{29,30} although sparing subregions implicated in full-body behaviors including the magnocellular and gigantocellular nucleus.^{46–48} In contrast, the majority of cortico-spinal neurons resides more caudally and establishes much sparser medullary collaterals. Focusing on anterior cortical territory, neurons with no spinal projections need to mandatorily signal through medullary circuits, as an intermediate signaling center to influence forelimb movement, without direct access to spinal circuits.

Our findings demonstrate that in mice, at a first level of organization, AC preferentially innervates forelimb-related medulla regions and is further subdivided according to its overall interaction hierarchies with medulla and/or spinal cord. A second level of organization relates to how synaptic input from different cortical domains terminates within the medulla. In the rostral medulla, cortical synaptic terminals tile the lateral domain from ventral to dorsal, with MAC elaborating its synaptic input most ventrally, neighbored by LAC input more dorsally, and InsC input most dorsally along this axis. Strikingly, these dorso-ventrally arranged synaptic sites of highest density extend along the length of the medulla, thereby generating 3D synaptic columns of shared cortical origin. Through this signaling strategy, cortical neurons can contact medulla neurons across distinct neuroanatomical domains of its rostral-caudal axis, thereby providing precisely organized parallel top-down synaptic input.

Organization of cortical input to medulla matches behavioral tuning of its neurons

A key question is whether and how the striking anatomical organization observed between cortex and medulla underlies functional organization. We found that MAC optogenetic stimulation elicits short latency excitatory responses preferentially in latRM neurons tuned to forelimb reaching but not handling phases of the pellet task. We also found that acute MAC silencing selectively disrupts reaching associated phases but not handling, compatible with previous work in which optogenetic inactivation of cortical sites within MAC but not of neighboring regions blocks reaching initiation and diverts ongoing reaching.³⁹ Noteworthy also, layer 2/3 neurons in this part of the cortex are tuned to directionality of forelimb reaches,³⁹ a property also exhibited by some latRM neurons.³⁰ In contrast, we found that LAC silencing disrupts food handling but not reaching and that LAC neurons connect preferentially to handling tuned but not reaching tuned latRM neurons. Interestingly, different regions within LAC, notably its most anterior (referred to as anterior lateral motor cortex [ALM]) and lateral domain (referred to as tongue/jaw motor cortex [tjM1]) were previously studied in the context of orofacial behaviors including licking^{15,17,20} or singing⁴⁹ (Figure S1A). Thus, further topography may exist within LAC to coordinate orofacial movements and handling related forelimb movements, behaviors frequently occurring jointly when mice consume food, through activity within LAC subregions and downstream connected circuits. This hypothesis is in agreement with work mapping the functional impact of cortical stimulation sites in head-fixed mice through optogenetics, eliciting a variety of muscle contraction patterns involving both orofacial and forelimb muscles, as well as forelimb movements toward the mouth similar to the ones occurring during food handling.¹⁶

Moreover, neurons presynaptic to motor neurons innervating orofacial muscles also reside in the medulla,¹⁶ making it plausible that LAC cortico-medullary neurons have access to these pathways as well and that different subregions of LAC might have functionally distinct targets within latRM. Together, these combined studies lend support to a model in which the influence of MAC is primarily on preparation and execution of forelimb reaching and trajectory elaboration, whereas LAC produces top-down modulation to coordinate forelimb handling and orofacial behaviors.

Our findings resonate with recent work on the organization of communication pathways within the medulla and to the spinal cord. Excitatory neurons in the latRM stratify into at least four anatomically distinct subpopulations based on their axonal projections and these populations can serve as an entry point to elicit distinct forelimb behaviors by optogenetic stimulation.³⁰ Excitatory latRM neurons projecting to the spinal cord are anatomically distinct from two groups of latRM neurons terminating in the caudal medulla. Although spinally projecting latRM neurons elicit forelimb reaching behavior, more complex and digit-involving forelimb movements including hand-to-mouth or grooming are elicited by stimulation of the latter populations.³⁰ Moreover, excitatory neurons in the medullary reticular nucleus, ventral part (MdV) located in the caudal medulla are required for the grasping but not reaching phase of the pellet task.²⁹ Thus, intra-medulla information processing appears to generate forelimb movements more complex than reaching, and therefore, top-down impact of LAC exclusively to this region rather than in addition directly to the spinal cord might serve the purpose of diversifying complex forelimb behaviors and perhaps also allowing for more behavioral flexibility and adjustments not least because coordination of forelimb and orofacial movement from within this caudal brainstem structure is strategically best placed. In contrast, forelimb reaching behavior has also behavioral manifestations independent of feeding, including the need for direct sensory feedback at the level of the spinal cord itself. Processing circuits for action control would therefore be most conveniently placed directly in the spinal cord, where also somatosensory feedback from limbs can impact reaching trajectories. The striking anatomical and functional pairing of cortico-medulla projection neurons residing in distinct cortical regions with behavioral-phase tuned neurons in the medulla provides insight into the principles of how the cortex communicates differentially through fine-grained functionally distinct channels with medullary and spinal circuits very close to the generation of movement.

This logic of organization might not only be suitable to influence the execution of behavioral phases but also has the potential to be involved in learning new movements involving forelimbs where instructions for learned content might be transferred to subcortical populations by modifying connectivity patterns through plasticity, similar to modifications occurring in the striatum.²² Inspection of synaptic arborization patterns of single reconstructed cortical neurons in the medulla shows tremendous differences ranging from very few synaptic boutons to large arbors with many sites. Analysis of these patterns across learning and functional recovery after injury or stroke has the potential to reveal whether and how these processes might modify connectivity at the intersection between cortex and medulla.

Limitations of the study

Our study addresses the acute role of MAC and LAC in skilled forelimb execution. It leaves open the question of whether this role can be assigned specifically to medulla-projecting MAC and LAC populations. Experiments silencing specifically these subpopulations of projection neurons would be a first step to address this question. However, such experiments are challenging due to lacking techniques to efficiently target a sufficiently large population of neurons in adult mice. Moreover, since we and others³³ demonstrated that medulla-projecting cortical neurons also exhibit collaterals to other subcortical structures, one could not exclude an indirect functional impact through other structures as we will argue below.

Because of the widespread axonal arborization of cortical output neurons and the diversity of cortical neurons, it is crucial to elucidate principles of synaptic interaction between cortex and subcortical structures at the level of defined populations. Indeed, the analysis of visual cortex single neuron long-range projections has revealed that most neurons innervate multiple targets but that there is an emerging logic with respect to target identity rather than a selection of random targets.⁵⁰ Our analysis of synaptic output patterns specifically from cortical neurons projecting to the medulla demonstrated that cortical populations establishing distinct channels to medullary subregions also do so at the same time to other levels in the motor system hierarchy. How the different collateral pathways established along the motor system by one population of cortico-medullary neurons collaborate in the production and learning of movement will be an interesting avenue to pursue in the future. It might however be difficult to disentangle the precise impact of these projection neurons on different subcortical targets.

The logic of organization might be similar to one revealed recently within basal ganglia circuits, where striatal projection neurons of the direct pathway use parallel communication channels for axon collaterals to the intermediate processing station globus pallidus externa (GPe), but exhibit a more convergent mode of communication to its output layer in the SNr.⁵¹ Moreover, even within similar overall arborization to a region, specific neuronal subtypes can establish preferential synaptic contacts with subsets of neurons in the target region, as was recently shown to occur for connectivity of cortico-spinal neurons to striatal neurons.⁴² Our work advances this understanding in demonstrating the precisely matched functional organization between different cortical regions and brainstem centers involved in the regulation of skilled forelimb movements. Future work will reveal how strategies of convergent and divergent signaling modes contribute to computations in the motor system across its hierarchy.

STAR★METHODS

Detailed methods are provided in the online version of this paper and include the following:

- KEY RESOURCES TABLE
- RESOURCE AVAILABILITY
 - Lead contact
 - Materials availability
 - Data and code availability

- **EXPERIMENTAL MODEL AND SUBJECT DETAILS**
 - Animals
- **METHOD DETAILS**
 - Virus production and surgical procedures
 - Immunohistochemistry and microscopy
 - Behavioral experiments
 - Electrophysiological recordings
- **QUANTIFICATION AND STATISTICAL ANALYSIS**
 - Anatomical reconstructions and analysis
 - MouseLight database analysis
 - Behavioral analysis of forelimb movements
 - Analysis of electrophysiological recordings
 - Statistics

SUPPLEMENTAL INFORMATION

Supplemental information can be found online at <https://doi.org/10.1016/j.cell.2022.12.009>.

ACKNOWLEDGMENTS

We are grateful to M. Sigrist, M. Mielich, C. Nyerges, A. Schwarzmüller, A. Gerber, T. Brumm, and S. Voggensperger for expert experimental help; to K. Bhandari and P. Caroni for help and advice with loss-of-function experiments; to P. Caroni, F. Donato, B. Roska, and A. Falasconi for discussions and comments on the manuscript; and to all members of the Arber laboratory for feedback throughout the project. W.Y. and H.K. were supported by a Biozentrum PhD Fellowship, and all authors by an ERC Advanced Grant (no. 692617), the Swiss National Science Foundation, the Kanton Basel-Stadt, the Novartis Research Foundation, and the Louis Jeantet Prize for Medicine.

AUTHOR CONTRIBUTIONS

All authors were involved in the design of experiments and data analysis. W.Y. carried out most anatomy experiments, and these were analyzed jointly by W.Y. and H.K. Neuronal recording and functional experiments were carried out jointly by W.Y. and H.K. and were analyzed by H.K. with contributions from W.Y. S.A. initiated the project and wrote the manuscript with contributions from W.Y. and H.K. All authors discussed the experiments and commented on the manuscript.

DECLARATION OF INTERESTS

The authors declare no competing interests.

Received: July 12, 2022

Revised: October 10, 2022

Accepted: December 5, 2022

Published: January 5, 2023

REFERENCES

1. Lemon, R.N. (2008). Descending pathways in motor control. *Annu. Rev. Neurosci.* 31, 195–218. <https://doi.org/10.1146/annurev.neuro.31.060407.125547>.
2. BRAIN Initiative Cell Census Network (BICCN) (2021). A multimodal cell census and atlas of the mammalian primary motor cortex. *Nature* 598, 86–102. <https://doi.org/10.1038/s41586-021-03950-0>.
3. Di Bella, D.J., Habibi, E., Stickels, R.R., Scalia, G., Brown, J., Yadollahpour, P., Yang, S.M., Abbate, C., Biancalani, T., Macosko, E.Z., et al. (2021). Molecular logic of cellular diversification in the mouse cerebral cortex. *Nature* 595, 554–559. <https://doi.org/10.1038/s41586-021-03670-5>.
4. Winnubst, J., Bas, E., Ferreira, T.A., Wu, Z., Economo, M.N., Edson, P., Arthur, B.J., Bruns, C., Rokicki, K., Schauder, D., et al. (2019). Reconstruction of 1,000 projection neurons reveals new cell types and organization of long-range connectivity in the mouse brain. *Cell* 179, 268–281.e13. <https://doi.org/10.1016/j.cell.2019.07.042>.
5. Graziano, M.S., Taylor, C.S., Moore, T., and Cooke, D.F. (2002). The cortical control of movement revisited. *Neuron* 36, 349–362. [https://doi.org/10.1016/s0896-6273\(02\)01003-6](https://doi.org/10.1016/s0896-6273(02)01003-6).
6. Tennant, K.A., Adkins, D.L., Donlan, N.A., Asay, A.L., Thomas, N., Kleim, J.A., and Jones, T.A. (2011). The organization of the forelimb representation of the C57BL/6 mouse motor cortex as defined by intracortical microstimulation and cytoarchitecture. *Cereb. Cortex* 21, 865–876. <https://doi.org/10.1093/cercor/bhq159>.
7. Ferezou, I., Haiss, F., Gentet, L.J., Aronoff, R., Weber, B., and Petersen, C.C. (2007). Spatiotemporal dynamics of cortical sensorimotor integration in behaving mice. *Neuron* 56, 907–923. <https://doi.org/10.1016/j.neuron.2007.10.007>.
8. Wang, X., Liu, Y., Li, X., Zhang, Z., Yang, H., Zhang, Y., Williams, P.R., Alwahaab, N.S.A., Kapur, K., Yu, B., et al. (2017). Deconstruction of corticospinal circuits for goal-directed motor skills. *Cell* 171, 440–455.e14. <https://doi.org/10.1016/j.cell.2017.08.014>.
9. Guo, J.Z., Graves, A.R., Guo, W.W., Zheng, J., Lee, A., Rodríguez-González, J., Li, N., Macklin, J.J., Phillips, J.W., Mensh, B.D., et al. (2015). Cortex commands the performance of skilled movement. *eLife* 4, e10774. <https://doi.org/10.7554/eLife.10774>.
10. Peters, A.J., Lee, J., Hedrick, N.G., O’Neil, K., and Komiyama, T. (2017). Reorganization of corticospinal output during motor learning. *Nat. Neurosci.* 20, 1133–1141. <https://doi.org/10.1038/nn.4596>.
11. Morandell, K., and Huber, D. (2017). The role of forelimb motor cortex areas in goal directed action in mice. *Sci. Rep.* 7, 15759. <https://doi.org/10.1038/s41598-017-15835-2>.
12. Mathis, M.W., Mathis, A., and Uchida, N. (2017). Somatosensory cortex plays an essential role in forelimb motor adaptation in mice. *Neuron* 93, 1493–1503.e6. <https://doi.org/10.1016/j.neuron.2017.02.049>.
13. Matyas, F., Sreenivasan, V., Marbach, F., Wacongne, C., Barsy, B., Mateo, C., Aronoff, R., and Petersen, C.C. (2010). Motor control by sensory cortex. *Science* 330, 1240–1243. <https://doi.org/10.1126/science.1195797>.
14. Sreenivasan, V., Karmakar, K., Rijli, F.M., and Petersen, C.C. (2015). Parallel pathways from motor and somatosensory cortex for controlling whisker movements in mice. *Eur. J. Neurosci.* 41, 354–367. <https://doi.org/10.1111/ejn.12800>.
15. Li, N., Chen, T.W., Guo, Z.V., Gerfen, C.R., and Svoboda, K. (2015). A motor cortex circuit for motor planning and movement. *Nature* 519, 51–56. <https://doi.org/10.1038/nature14178>.
16. Mercer Lindsay, N., Knutsen, P.M., Lozada, A.F., Gibbs, D., Karten, H.J., and Kleinfeld, D. (2019). Orofacial movements involve parallel corticobulbar projections from motor cortex to trigeminal premotor nuclei. *Neuron* 104, 765–780.e3. <https://doi.org/10.1016/j.neuron.2019.08.032>.
17. Mayrhofer, J.M., El-Boustani, S., Foustoukos, G., Auffret, M., Tamura, K., and Petersen, C.C.H. (2019). Distinct contributions of whisker sensory cortex and tongue-jaw motor cortex in a goal-directed sensorimotor transformation. *Neuron* 103, 1034–1043.e5. <https://doi.org/10.1016/j.neuron.2019.07.008>.
18. Peters, A.J., Chen, S.X., and Komiyama, T. (2014). Emergence of reproducible spatiotemporal activity during motor learning. *Nature* 510, 263–267. <https://doi.org/10.1038/nature13235>.
19. Kawai, R., Markman, T., Poddar, R., Ko, R., Fantana, A.L., Dhawale, A.K., Kampff, A.R., and Ölveczky, B.P. (2015). Motor cortex is required for learning but not for executing a motor skill. *Neuron* 86, 800–812. <https://doi.org/10.1016/j.neuron.2015.03.024>.
20. Bollu, T., Ito, B.S., Whitehead, S.C., Kardon, B., Redd, J., Liu, M.H., and Goldberg, J.H. (2021). Cortex-dependent corrections as the tongue reaches for and misses targets. *Nature* 594, 82–87. <https://doi.org/10.1038/s41586-021-03561-9>.

21. Heindorf, M., Arber, S., and Keller, G.B. (2018). Mouse motor cortex coordinates the behavioral response to unpredicted sensory feedback. *Neuron* 99, 1040–1054.e5. <https://doi.org/10.1016/j.neuron.2018.07.046>.
22. Lemke, S.M., Ramanathan, D.S., Guo, L., Won, S.J., and Ganguly, K. (2019). Emergent modular neural control drives coordinated motor actions. *Nat. Neurosci.* 22, 1122–1131. <https://doi.org/10.1038/s41593-019-0407-2>.
23. Alexander, G.E., DeLong, M.R., and Strick, P.L. (1986). Parallel organization of functionally segregated circuits linking basal ganglia and cortex. *Annu. Rev. Neurosci.* 9, 357–381. <https://doi.org/10.1146/annurev.ne.09.030186.002041>.
24. Hintiryan, H., Foster, N.N., Bowman, I., Bay, M., Song, M.Y., Gou, L., Yamashita, S., Bienkowski, M.S., Zingg, B., Zhu, M., et al. (2016). The mouse cortico-striatal projectome. *Nat. Neurosci.* 19, 1100–1114. <https://doi.org/10.1038/nn.4332>.
25. Peters, A.J., Fabre, J.M.J., Steinmetz, N.A., Harris, K.D., and Carandini, M. (2021). Striatal activity topographically reflects cortical activity. *Nature* 591, 420–425. <https://doi.org/10.1038/s41586-020-03166-8>.
26. Yakovenko, S., Krouchev, N., and Drew, T. (2011). Sequential activation of motor cortical neurons contributes to intralimb coordination during reaching in the cat by modulating muscle synergies. *J. Neurophysiol.* 105, 388–409. <https://doi.org/10.1152/jn.00469.2010>.
27. Hyland, B.I., and Jordan, V.M. (1997). Muscle activity during forelimb reaching movements in rats. *Behav. Brain Res.* 85, 175–186. [https://doi.org/10.1016/s0166-4328\(97\)87582-1](https://doi.org/10.1016/s0166-4328(97)87582-1).
28. Iwaniuk, A.N., and Whishaw, I.Q. (2000). On the origin of skilled forelimb movements. *Trends Neurosci.* 23, 372–376. [https://doi.org/10.1016/s0166-2236\(00\)01618-0](https://doi.org/10.1016/s0166-2236(00)01618-0).
29. Esposito, M.S., Capelli, P., and Arber, S. (2014). Brainstem nucleus MdV mediates skilled forelimb motor tasks. *Nature* 508, 351–356. <https://doi.org/10.1038/nature13023>.
30. Ruder, L., Schina, R., Kanodia, H., Valencia-Garcia, S., Pivetta, C., and Arber, S. (2021). A functional map for diverse forelimb actions within brainstem circuitry. *Nature* 590, 445–450. <https://doi.org/10.1038/s41586-020-03080-z>.
31. Lemon, R.N., Landau, W., Tutssel, D., and Lawrence, D.G. (2012). Lawrence and Kuypers (1968a, b) revisited: copies of the original filmed material from their classic papers in *Brain*. *Brain* 135, 2290–2295. <https://doi.org/10.1093/brain/aws037>.
32. Shepherd, G.M. (2013). Corticostriatal connectivity and its role in disease. *Nat. Rev. Neurosci.* 14, 278–291. <https://doi.org/10.1038/nrn3469>.
33. Economo, M.N., Viswanathan, S., Tasic, B., Bas, E., Winnubst, J., Menon, V., Graybiack, L.T., Nguyen, T.N., Smith, K.A., Yao, Z., et al. (2018). Distinct descending motor cortex pathways and their roles in movement. *Nature* 563, 79–84. <https://doi.org/10.1038/s41586-018-0642-9>.
34. Inagaki, H.K., Chen, S., Ridder, M.C., Sah, P., Li, N., Yang, Z., Hasanbegovic, H., Gao, Z., Gerfen, C.R., and Svoboda, K. (2022). A midbrain-thalamus-cortex circuit reorganizes cortical dynamics to initiate movement. *Cell* 185, 1065–1081.e23. <https://doi.org/10.1016/j.cell.2022.02.006>.
35. Tervo, D.G., Hwang, B.Y., Viswanathan, S., Gaj, T., Lavzin, M., Ritola, K.D., Lindo, S., Michael, S., Kuleshova, E., Ojala, D., et al. (2016). A designer AAV variant permits efficient retrograde access to projection neurons. *Neuron* 92, 372–382. <https://doi.org/10.1016/j.neuron.2016.09.021>.
36. Franklin, K.B., and Paxinos, G. (2007). *The Mouse Brain in Stereotaxic Coordinates, Third Edition* (Elsevier).
37. Kamiyama, T., Kameda, H., Murabe, N., Fukuda, S., Yoshioka, N., Mizukami, H., Ozawa, K., and Sakurai, M. (2015). Corticospinal tract development and spinal cord innervation differ between cervical and lumbar targets. *J. Neurosci.* 35, 1181–1191. <https://doi.org/10.1523/JNEUROSCI.2842-13.2015>.
38. Mathis, A., Mamidanna, P., Cury, K.M., Abe, T., Murthy, V.N., Mathis, M.W., and Bethge, M. (2018). DeepLabCut: markerless pose estimation of user-defined body parts with deep learning. *Nat. Neurosci.* 21, 1281–1289. <https://doi.org/10.1038/s41593-018-0209-y>.
39. Galiñanes, G.L., Bonardi, C., and Huber, D. (2018). Directional reaching for water as a cortex-dependent behavioral framework for mice. *Cell Rep.* 22, 2767–2783. <https://doi.org/10.1016/j.celrep.2018.02.042>.
40. Zingg, B., Chou, X.L., Zhang, Z.G., Mesik, L., Liang, F., Tao, H.W., and Zhang, L.I. (2017). AAV-mediated anterograde transsynaptic tagging: mapping corticocollicular input-defined neural pathways for defense behaviors. *Neuron* 93, 33–47. <https://doi.org/10.1016/j.neuron.2016.11.045>.
41. Zingg, B., Peng, B., Huang, J., Tao, H.W., and Zhang, L.I. (2020). Synaptic specificity and application of anterograde transsynaptic AAV for probing neural circuitry. *J. Neurosci.* 40, 3250–3267. <https://doi.org/10.1523/JNEUROSCI.2158-19.2020>.
42. Nelson, A., Abdelmesih, B., and Costa, R.M. (2021). Corticospinal populations broadcast complex motor signals to coordinated spinal and striatal circuits. *Nat. Neurosci.* 24, 1721–1732. <https://doi.org/10.1038/s41593-021-00939-w>.
43. Ueno, M., Nakamura, Y., Li, J., Gu, Z., Niehaus, J., Maezawa, M., Crone, S.A., Goulding, M., Bacceti, M.L., and Yoshida, Y. (2018). Corticospinal circuits from the sensory and motor cortices differentially regulate skilled movements through distinct spinal interneurons. *Cell Rep.* 23, 1286–1300.e7. <https://doi.org/10.1016/j.celrep.2018.03.137>.
44. Sahni, V., Shnyder, S.J., Jabaudon, D., Song, J.H.T., Itoh, Y., Greig, L.C., and Macklis, J.D. (2021). Corticospinal neuron subpopulation-specific developmental genes prospectively indicate mature segmentally specific axon projection targeting. *Cell Rep.* 37, 109843. <https://doi.org/10.1016/j.celrep.2021.109843>.
45. Morecraft, R.J., Ge, J., Stilwell-Morecraft, K.S., McNeal, D.W., Pizzimenti, M.A., and Darling, W.G. (2013). Terminal distribution of the corticospinal projection from the hand/arm region of the primary motor cortex to the cervical enlargement in rhesus monkey. *J. Comp. Neurol.* 521, 4205–4235. <https://doi.org/10.1002/cne.23410>.
46. Cregg, J.M., Leiras, R., Montalant, A., Wanken, P., Wickersham, I.R., and Kiehn, O. (2020). Brainstem neurons that command mammalian locomotor asymmetries. *Nat. Neurosci.* 23, 730–740. <https://doi.org/10.1038/s41593-020-0633-7>.
47. Usseglio, G., Gatier, E., Heuzé, A., Hérent, C., and Bouvier, J. (2020). Control of orienting movements and locomotion by projection-defined subsets of brainstem V2a neurons. *Curr. Biol.* 30, 4665–4681.e6. <https://doi.org/10.1016/j.cub.2020.09.014>.
48. Capelli, P., Pivetta, C., Esposito, M.S., and Arber, S. (2017). Locomotor speed control circuits in the caudal brainstem. *Nature* 551, 373–377. <https://doi.org/10.1038/nature24064>.
49. Okobi, D.E., Jr., Banerjee, A., Matheson, A.M.M., Phelps, S.M., and Long, M.A. (2019). Motor cortical control of vocal interaction in Neotropical singing mice. *Science* 363, 983–988. <https://doi.org/10.1126/science.aau9480>.
50. Han, Y., Kebschull, J.M., Campbell, R.A.A., Cowan, D., Imhof, F., Zador, A.M., and Mrsic-Flogel, T.D. (2018). The logic of single-cell projections from visual cortex. *Nature* 556, 51–56. <https://doi.org/10.1038/nature26159>.
51. Foster, N.N., Barry, J., Korobkova, L., Garcia, L., Gao, L., Becerra, M., Sherafat, Y., Peng, B., Li, X., Choi, J.H., et al. (2021). The mouse cortico-basal ganglia-thalamic network. *Nature* 598, 188–194. <https://doi.org/10.1038/s41586-021-03993-3>.
52. Takeoka, A., Vollenweider, I., Courtine, G., and Arber, S. (2014). Muscle spindle feedback directs locomotor recovery and circuit reorganization after spinal cord injury. *Cell* 159, 1626–1639. <https://doi.org/10.1016/j.cell.2014.11.019>.
53. Basaldella, E., Takeoka, A., Sigrist, M., and Arber, S. (2015). Multisensory signaling shapes vestibulo-motor circuit specificity. *Cell* 163, 301–312. <https://doi.org/10.1016/j.cell.2015.09.023>.

54. Ferreira-Pinto, M.J., Kanodia, H., Falasconi, A., Sigrist, M., Esposito, M.S., and Arber, S. (2021). Functional diversity for body actions in the mesencephalic locomotor region. *Cell* 184, 4564–4578.e18. <https://doi.org/10.1016/j.cell.2021.07.002>.
55. Pivetta, C., Esposito, M.S., Sigrist, M., and Arber, S. (2014). Motor-circuit communication matrix from spinal cord to brainstem neurons revealed by developmental origin. *Cell* 156, 537–548. <https://doi.org/10.1016/j.cell.2013.12.014>.
56. Cao, V.Y., Ye, Y., Mastwal, S., Ren, M., Coon, M., Liu, Q., Costa, R.M., and Wang, K.H. (2015). Motor learning consolidates arc-expressing neuronal ensembles in secondary motor cortex. *Neuron* 86, 1385–1392. <https://doi.org/10.1016/j.neuron.2015.05.022>.
57. Otchy, T.M., Wolff, S.B., Rhee, J.Y., Pehlevan, C., Kawai, R., Kempf, A., Gobes, S.M., and Ölveczky, B.P. (2015). Acute off-target effects of neural circuit manipulations. *Nature* 528, 358–363. <https://doi.org/10.1038/nature16442>.
58. Xu, T., Yu, X., Perlik, A.J., Tobin, W.F., Zweig, J.A., Tennant, K., Jones, T., and Zuo, Y. (2009). Rapid formation and selective stabilization of synapses for enduring motor memories. *Nature* 462, 915–919. <https://doi.org/10.1038/nature08389>.
59. Tinevez, J.Y., Perry, N., Schindelin, J., Hoopes, G.M., Reynolds, G.D., Laplantine, E., Bednarek, S.Y., Shorte, S.L., and Eliceiri, K.W. (2017). TrackMate: an open and extensible platform for single-particle tracking. *Methods* 115, 80–90. <https://doi.org/10.1016/j.ymeth.2016.09.016>.
60. Takatoh, J., Park, J.H., Lu, J., Li, S., Thompson, P.M., Han, B.X., Zhao, S., Kleinfeld, D., Friedman, B., and Wang, F. (2021). Constructing an adult orofacial premotor atlas in Allen mouse CCF. *eLife* 10. <https://doi.org/10.7554/eLife.67291>.
61. Shamash, P., Carandini, M., Harris, K., and Steinmetz, N.A. (2018). A tool for analyzing electrode tracks from slice histology <https://doi.org/10.1101/447995>.
62. Claudi, F., Tyson, A.L., Petrucco, L., Margrie, T.W., Portugues, R., and Branco, T. (2021). Visualizing anatomically registered data with brainrender. *eLife* 10, e65751. <https://doi.org/10.7554/eLife.65751>.
63. Morita, K., Im, S., and Kawaguchi, Y. (2019). Differential striatal axonal arborizations of the intratelencephalic and pyramidal-tract neurons: analysis of the data in the MouseLight database. *Front. Neural Circuits* 13, 71. <https://doi.org/10.3389/fncir.2019.00071>.
64. Lopes, G., Bonacchi, N., Frazão, J., Neto, J.P., Atallah, B.V., Soares, S., Moreira, L., Matias, S., Itskov, P.M., Correia, P.A., et al. (2015). Bonsai: an event-based framework for processing and controlling data streams. *Front. Neuroinform.* 9, 7. <https://doi.org/10.3389/fninf.2015.00007>.
65. Jun, J.J., Steinmetz, N.A., Siegle, J.H., Denman, D.J., Bauza, M., Barbarits, B., Lee, A.K., Anastassiou, C.A., Andrei, A., Aydın, Ç., et al. (2017). Fully integrated silicon probes for high-density recording of neural activity. *Nature* 551, 232–236. <https://doi.org/10.1038/nature24636>.
66. Pachirariu, M., Steinmetz, N.A., Kadir, S., Carandini, M., and Harris, K.D. (2016). Kilosort: realtime spike-sorting for extracellular electrophysiology with hundreds of channels. *bioRxiv*. <https://doi.org/10.1101/061481>.
67. Wang, Q., Ding, S.L., Li, Y., Royall, J., Feng, D., Lesnar, P., Graddis, N., Naeemi, M., Facer, B., Ho, A., et al. (2020). The Allen Mouse Brain Common coordinate framework: A 3D reference atlas. *Cell* 181, 936–953.e20. <https://doi.org/10.1016/j.cell.2020.04.007>.

STAR★METHODS

KEY RESOURCES TABLE

REAGENT or RESOURCE	SOURCE	IDENTIFIER
Antibodies		
chicken anti-GFP	Invitrogen	Cat# A10262; RRID: AB_2534023
chicken anti-Myc	Invitrogen	Cat# A21281; RRID: AB_2535826
Rabbit anti-GFAP	Millipore	Cat# AB5804; RRID: AB_2109645
goat anti-ChAT	Millipore	Cat# AB144P; RRID: AB_2079751
mouse anti-V5	Invitrogen	Cat# R960CUS; RRID: AB_2792973
rabbit anti-RFP	Rockland	Cat# 600-401-379; RRID: AB_2209751
Donkey anti-rabbit Cy3	Jackson Immuno Research	Cat#711-165-152; RRID: AB_2307443
Donkey anti-goat Cy5	Invitrogen	Cat# A-21447; RRID: AB_2535864
Donkey anti-chicken 488	Jackson Immuno Research	Cat#703-545-155; RRID: AB_2340375
Donkey anti-chicken Cy5	Jackson Immuno Research	Cat#703-605-155; RRID: AB_2340379
Donkey anti-goat 488	Invitrogen	Cat# A-11055; RRID: AB_2534102
Donkey anti-mouse 647	Invitrogen	Cat# A-31571; RRID: AB_162542
Donkey anti-mouse Cy3	Invitrogen	Cat# A-31570; RRID: AB_2536180
Donkey anti-mouse DyL405	Jackson Immuno Research	Cat# 715-475-150; RRID: AB_2340839
Virus strains		
AAV-flex-SynMyc	Pivetta et al. ⁵⁵	N/A
AAV-flex-TdTomato	Capelli et al. ⁴⁸	N/A
AAV-flex-H2B-V5	Ruder et al. ³⁰	N/A
AAV-H2B-10xMyc	Ruder et al. ³⁰	N/A
AAV-H2B-V5	Ruder et al. ³⁰	N/A
AAV-Cre	This study	N/A
AAV-Cre-H2B-GFP	This study	N/A
AAV-Cre-H2B-V5	This study	N/A
AAV-hChr2(H134R)-EYFP	Addgene	Addgene no. 20298
AAV-fDIO-EYFP	Addgene	Addgene no. 55641
AAV(1)-hSyn-Cre	Addgene	Addgene no. 105553
AAV(1)-hSyn-Flpo	Addgene	Addgene no. 60663
Experimental models: Organisms/strains		
Mouse: C57BL/6J	Charles River	Strain Code: 027
Software and algorithms		
MATLAB (v2017b)	Mathworks	https://www.mathworks.com/ RRID:SCR_001622

(Continued on next page)

Continued

REAGENT or RESOURCE	SOURCE	IDENTIFIER
Python (v3.7)	Python	https://www.python.org/ RRID:SCR_008394
CorelDraw (vX9)	Corel	https://www.coreldraw.com/ RRID:SCR_014235
Imaris (v9.1.2)	Oxford Instruments Group	http://www.bitplane.com/imaris/imaris RRID:SCR_007370
Bonsai (v2.3)	NeuroGEARS Ltd.	https://bonsai-rx.org RRID:SCR_017218
Fiji	Fiji	http://fiji.sc RRID:SCR_002285
TrackMate (v6.0.3)	TrackMate	https://imagej.net/plugins/trackmate/
Kilosort v2	Cortex lab	https://github.com/MouseLand/ Kilosort/releases/tag/v2.0
Kilosort v3	Cortex lab	https://github.com/MouseLand/Kilosort
Phy2	Cortex lab	https://github.com/cortex-lab/phy
DeepLabCut	Mathis Lab; Mathis et al. ³⁸	http://www.mousemotorlab.org/deeplabcut
Custom code for analysis of electrophysiology, anatomy and behavior	This paper	https://github.com/arberlab-wyhk/ Yang-et-al-2022

Deposited data

Primary data	This paper	https://doi.org/10.5281/zenodo.7363150
--------------	------------	---

Other

MouseLight database: AA0180	Janelia Research Campus	https://doi.org/10.25378/janelia.5527441
MouseLight database: AA0012	Janelia Research Campus	https://doi.org/10.25378/janelia.5521618
MouseLight database: AA0250	Janelia Research Campus	https://doi.org/10.25378/janelia.5527678
MouseLight database: AA0788	Janelia Research Campus	https://doi.org/10.25378/janelia.7739369
MouseLight database: AA0179	Janelia Research Campus	https://doi.org/10.25378/janelia.5527438
MouseLight database: AA0576	Janelia Research Campus	https://doi.org/10.25378/janelia.7649849
MouseLight database: AA0726	Janelia Research Campus	https://doi.org/10.25378/janelia.7707194
MouseLight database: AA1543	Janelia Research Campus	N/A
MouseLight database: AA0133	Janelia Research Campus	https://doi.org/10.25378/janelia.5527273
MouseLight database: AA0134	Janelia Research Campus	https://doi.org/10.25378/janelia.5527276
MouseLight database: AA0169	Janelia Research Campus	https://doi.org/10.25378/janelia.5527408
MouseLight database: AA1043	Janelia Research Campus	https://doi.org/10.25378/janelia.7822304
MouseLight database: AA0956	Janelia Research Campus	https://doi.org/10.25378/janelia.7804088
Muscimol	Tocris	Cat. No.0289
Beads, Fluoro-Max Dyed Blue Aqueous Fluorescent Particles	Thermo Scientific	Catalog number: B500
Fiber specs: (.39/200) – active length 0.5mm Implant length: 1.5mm	OptogeniX	https://www.optogenix.com/
ASSY-156-H5	Cambridge NeuroTech	https://www.cambridgeneurotech.com/
Neuropixels 1.0	IMEC	https://www.neuropixels.org/
RHD USB interface board	Intan Technologies	https://intantech.com/
NI PXIe-1071, 4-Slot 3U PXI Express Chassis	National instrument	https://www.ni.com/
NI PXIe-PCIe8381,x8 Gen2 MXI-Express for PXI Express Interface,3m	National instrument	https://www.ni.com/
PXIe-6341, X Series DAQ	National instrument	https://www.ni.com/
Neuropixels fixture	ATLAS Neuro	https://www.atlasneuro.com/

(Continued on next page)

Continued

REAGENT or RESOURCE	SOURCE	IDENTIFIER
FV1000 confocal microscope	Olympus	http://www.olympusconfocal.com/products/fv1000/index.html
ZEISS Axio Imager 2	Zeiss	https://www.zeiss.com/microscopy/int/products/light-microscopes/axio-imager-2-for-biology.html
CSU-W1 Confocal Scanner Unit	Yokogawa	https://www.yokogawa.com/solutions/products-platforms/life-science/spinning-disk-confocal/csu-w1-confocal-scanner-unit/
Ace 2 Area Scan Cameras	Basler AG	a2A1920-160umBAS
Cobolt 06-MLD; 473nm; 100mW	HÜBNER Photonics	https://hubner-photonics.com/products/lasers/diode-lasers/06-01-series/
Model 1900 Stereotaxic Alignment System	Kopf	http://kopfinstruments.com/product/model-1900-stereotaxic-alignment-system/
Mouse schemes	Zenodo, scidraw.io	https://doi.org/10.5281/zenodo.3926569 https://doi.org/10.5281/zenodo.3925937 https://doi.org/10.5281/zenodo.3925901

RESOURCE AVAILABILITY

Lead contact

Further information or requests for reagents and resources should be addressed to the lead contact, Silvia Arber (silvia.arber@unibas.ch).

Materials availability

All originally made constructs for AAV production described in this manuscript are available upon request by contacting the [lead contact](#).

Data and code availability

- Primary data for figures are made available at Zenodo and accession number is stated in the [key resources table](#). Microscopy data reported in this paper will be shared by the [lead contact](#) upon request.
- The custom code examples are made available in a GitHub repository stated in the [key resources table](#).
- Any additional information required to reanalyze the data reported in this work is available from the [lead contact](#) upon request.

EXPERIMENTAL MODEL AND SUBJECT DETAILS

Animals

We used wild-type C57BL/6J mice from Charles River. For behavioral experiments, we used 2-4 month-old male mice, individually housed with horizontal running wheels. For anatomical experiments, both male and female mice of 2-4 months were used. Experimental mice originating from different litters were used in individual experiments. No criteria were applied to allocate mice to experimental groups. All procedures pertaining to housing, surgery, behavioral experiments and euthanasia were approved by the Cantonal Veterinary Office Basel-Stadt and performed in compliance with the Swiss Veterinary Law guidelines.

METHOD DETAILS

Virus production and surgical procedures

The following, previously described adeno-associated viruses (AAV), all based on a backbone derived from Allen Brain (AAV-CAG-flex-tdTomato-WPRE-bGH): AAV-flex-SynMyc (referred to as AAV-flex-SynTag),⁵² AAV-flex-tdTomato (referred to as AAV-flex-CytTag),⁴⁸ AAV-H2B-10xMyc, AAV-H2B-V5 (referred to as AAV-nTag), AAV-flex-H2B-V5 (referred to as AAV-flex-nTag).³⁰ Not previously reported viral constructs were designed in analogy to above constructs: AAV-Cre-H2B-V5, AAV-Cre-H2B-GFP (referred to as AAV-Cre-nTag). AAV-EF1a-double floxed-hChR2(H134R)-EYFP (Addgene no. 20298) and AAV-Ef1a-fDIO-EYFP (Addgene no. 55641, referred to as AAV-*frt*-CytTag) were from Addgene. For unconditional expression of constructs using Cre-conditional AAVs, mice were co-injected with AAV-Cre. To infect neurons through local infection, a 2.9 serotype plasmid was used for production as in previous studies.^{29,30,53-55} For retrograde targeting of neurons by means of axonal infection, a rAAV2-

retro capsid plasmid³⁵ was used for coating as described previously.^{30,48,54} For transsynaptic targeting of postsynaptic recipient neurons from cortex, a 2.1 serotype^{40,41} was used to produce AAV(1)-hSyn-Cre (Addgene no. 105553) or AAV(1)-hSyn-Flpo (Addgene no. 60663). All AAVs used in this study were produced following standard protocols. Genomic titers for rAAV2-retro and AAV2.1 were between 1–5x10¹³, and for AAV2.9 were between 1x10¹² to 1x10¹³.

Buprenorphine (Temgesic, 0.1mg/kg) was applied subcutaneously as pre-emptive analgesia half an hour before beginning of surgery. Mice were anaesthetized with 2–3% isoflurane using oxygen as a gas carrier. Depth of anesthesia was controlled by testing the foot reflex and breathing movement. Once deeply anesthetized, mice were transferred to the stereotaxic frame under 1–2% isoflurane. Anesthesia was kept constant by regulating the isoflurane concentration. Surgical equipment was disinfected and a heating pad was used during the surgical procedures to avoid body temperature to drop. Eyes were protected from dehydration with ocular gel. Mice were injected with a mixture (50:50) of Lidocaine (10mg/kg) and Ropivacaine (Naropin, 3mg/kg) in the area of the surgery to reduce post-operative pain. Once anesthetized, the skin is shaved and disinfected. After surgery, Buprenorphine (0.1mg/kg) was applied subcutaneously on the day of the surgery, followed by subcutaneous injection of Meloxicam (Metacam, 5 mg/kg) at awakening to assure analgesia and for the next two days at an interval of 24 hours.

Viruses were delivered to the target brain regions via stereotaxic injection with high precision stereotaxic instruments (Kopf Instruments, Model 1900). Stereotaxic coordinates for brain injections are defined as antero-posterior (AP), medio-lateral (ML) and dorso-ventral (DV) (AP; ML; DV; in mm; approximate injection volumes: 50–100nl), taking lambda as a reference for the AP and ML axis for medulla injections, while bregma was used as a reference point for the AP and ML axis for cortex: latRM (-1.4; -1.55; -4.7); MAC (1.8; 1; 0.8); LAC (1.8; 2; 0.8); InsC (0; 3.9; 3). Injections in the spinal cord were targeted to either the cervical segments C5–C8 or the lumbar segments L1–L3 with an approximate injection volume of 300–500nl. Retrograde tracings to map the location of cortical neurons with defined outputs using rAAV2-retro-nTag or rAAV2-retro-Cre-nTag viruses were carried out by injections in the spinal cord or latRM. For systematically mapping the cortical output, we injected a mixture (2:2:1:1) of AAV-flex-SynMyc (to visualize synaptic output), AAV-flex-tdTomato (to show neuronal processes including axons), AAV-flex-H2B-V5 (to reveal the extent of the injection site), AAV-Cre (to allow the expression of conditional viruses), and waited at least four weeks for expression before perfusion. The injection sites were designed to cover the areas defined by retrograde mapping experiments and the coordinates of the injection sites were measured by *post hoc* assessment based on cortical spreading of the nuclear tag signal. For mapping the recipient neurons targeted by the cortex, AAV(1)-hSyn-Cre and AAV(1)-hSyn-Flpo were injected into two cortical regions (MAC/LAC or LAC/InsC), respectively. A mixture (1:1) of AAV(9)-flex-tdTomato and AAV(9)-Ef1a-fDIO-EYFP was injected into latRM. To specifically label the latRM projecting cortical neurons, rAAV2-retro-Cre-nTag virus was injected in latRM, and a mixture (1:1) of AAV(9)-flex-tdTomato and AAV-flex-SynMyc in the cortex.

For cortex inactivation, application sites were accessed with high precision stereotaxic instruments. The coordinates were as follows (AP; ML; in mm): MAC (1.8; ±1); LAC (1.8; ±2). Injections were performed as previously described.^{56,57} Briefly, 100 nl of 25 mM solution (Tocris, Cat. No.0289) was injected into a cortical site at a depth of 0.8mm from dura, together with beads (Thermo Scientific, Cat. No. B500) to verify precision of injection sites. For control, sites were injected with PBS.

For optogenetic cortex activation during electrophysiological recordings from mice in the latRM, we performed unilateral injection with AAV-flex-ChR2 and AAV-Cre into the cortex (coordinates of MAC and LAC same as above). One week thereafter, mice were trained in the pellet reaching task (see Behavior experiments) for one week.

Immunohistochemistry and microscopy

All mice in this study from anatomical and behavior experiments were euthanized, and brains and spinal cords were collected for histological processing, as previously described.⁴⁸ In brief, transcardial perfusion was performed under deep anesthesia with Ketamine-Xylazine. Anesthetized animals were first perfused with cold phosphate buffer saline (PBS) and subsequent fixation using a 4% paraformaldehyde (PFA) solution (Sigma). Brains and spinal cords were dissected, post-fixed overnight in 4% PFA, and incubated in 30% sucrose (w/v) in PBS for at least two days before cryopreservation. Brains and spinal cords were sliced at 80µm thickness on a cryostat (coronally for brain tissue and transversely for spinal cord). We collected floating sections sequentially into individual wells and incubated them for one-hour in blocking solution (1% BSA/0.2% TritonX100/PBS). Primary antibodies diluted in blocking solution were applied and incubated for 1–3 days at 4°C. Fluorophore-coupled secondary antibodies (Jackson or Invitrogen) were used for one-day incubations at 4°C, after extensive washing of tissue sections. After final washing, sections were mounted on glass slides in anti-bleach preservative medium in sequential order along the rostro-caudal axis. Primary antibodies used in this study were: chicken anti-GFP (Invitrogen), sheep anti GFP (Bio-Rad), chicken anti-Myc (Invitrogen), goat anti-ChAT (Millipore), mouse anti-V5 (Invitrogen) and rabbit anti-RFP (Rockland), rabbit anti-GFAP (Millipore). To acquire low-resolution overview images, we used an Axioscan light microscope (Zeiss, 5x objective) and for higher resolution imaging, we used a FV1000 confocal microscope (Olympus) or an Axio Imager M2 microscope (Zeiss) with a Yokogawa CSU W1 Dual camera T2 spinning disk confocal scanning unit.

Behavioral experiments

The pellet reaching and handling task was performed as previously described.^{29,30,58} Briefly, food-restricted mice were placed in a custom-made chamber containing a slit and trained to protrude the arm through the slit, reaching for a food reward. The body weight of mice was monitored to not drop below 85% of the original weight. Videos were recorded from below and side for pose estimation with Basler cameras (Ace 2 series). Mice were allowed to obtain food pellets with their tongue only on the first day, to accustom them

to the goal of retrieving food. On following days, mice were motivated to use the forelimb for reaching trials, by placing the food pellets at a marked, consistent position outside the slit further away and not accessible to the tongue. For loss-of-function experiments, mice were trained for at least 7 days aiming for a success rate of > 30% and with a goal of retrieving >15 pellets or 35 reaches. All mice (n=9) were included in analysis. Depending on whether mice were right- or left-handed, the pellet position was slightly moved to the side relative to the slit. For electrophysiological recording experiments, mice reaching with their left hand were trained for 7 days and only successful first attempt forelimb reaches were selected for analysis (see [electrophysiological recording](#)).

Electrophysiological recordings

To perform *in vivo* extracellular electrophysiological recordings, single-shank chronic 64-channel silicon probes (Cambridge NeuroTech Inc., H5, 0.8mm recording length) or Neuropixels probes (imec, NP1.0)⁶⁵ were implanted into the latRM contralateral to the side of cortex with virus injection. For implantation, a tapered optic fiber (OptogeniX, lambda fiber with 0.5mm active length, 0.39 numerical aperture and 200 μm diameter) was implanted on the cortex at the location of virus injection. Before probe implantation, Cambridge NeuroTech probes were mounted on a nanodrive (Cambridge NeuroTech Inc.), while Neuropixels probes were mounted on 3D printed fixtures (ATLAS Neuroengineering). The probe was then implanted in the latRM (AP and ML coordinates as for virus injections) at a dorso-ventral depth of around -4.9 mm using light curable cement (Relyx Unicem 2, 3M Inc.). We confirmed correct probe placement and location of recording sites after termination of experiments, by using ChAT immunohistochemistry (see Immunohistochemistry and microscopy) to visualize brainstem motor nuclei and electrodes ([Figure S5B](#); Neuropixels with thin layer of Dil, Invitrogen).

Extracellular electrophysiological data with the Cambridge Neurotech probes was recorded using the Intan 64 channel headstage at an acquisition rate of 30kHz. The camera exposure pulses and laser pulses, from which the timestamps of the camera video frames and laser start were extracted, were obtained aligned to the electrophysiology signal recorded on the Intan RHD USB interface.

QUANTIFICATION AND STATISTICAL ANALYSIS

Anatomical reconstructions and analysis

Viral injections and tissue processing were performed as described above (see Virus production and surgical procedures). To map the neuronal distribution of cortical populations stratified by projections to latRM or spinal cord, 80 μm thick coronal sections encompassing the full cortical area along its rostro-caudal axis were acquired using the Axioscan light microscope with a 5x objective. Every section along the rostro-caudal axis is used for analysis; the position where lateral ventricles begin to be separated was determined as bregma.³⁶ The depth of cortical neurons was obtained from 5 slices per mouse of the analyzed region and calculated based on the perpendicular distance of each neuron to the pia. To assess projections of cortical neurons to the medulla, superior colliculus, striatum, subthalamic/para-subthalamic nucleus, substantia nigra, and the position of postsynaptic neurons in the medulla receiving cortical input through anterograde virus transfer, 80 μm thick coronal sections were acquired with a 20x objective of a confocal microscope (FV 1000, Olympus) or an Axio Imager M2 microscope (Zeiss) with a Yokogawa CSU W1 Dual camera T2 spinning disk confocal scanning unit, tiling mosaics of multiple fields of view (z-step = 1.2 μm for synapses; = 5 μm for neurons). Three rostro-caudal levels were selected along the axis of the medulla for analysis.³⁶ The three chosen levels for analysis were as follows: rostral medulla at mid-7N level (Bregma -6mm)³⁰; caudal medulla at the hypoglossal (12N) level (Bregma -7.32mm)²⁹; intermediate medulla midway between these rostral and caudal medulla levels (Bregma -6.64mm).⁴⁸ Three rostro-caudal levels of striatum were selected based on striatal domain parcellations as previously reported,²⁴ i.e., Bregma +1.42mm, +0.14mm and -0.7mm. Two rostro-caudal levels of superior colliculus (Bregma -3.64mm and -4.04mm), three levels of subthalamic/para-subthalamic nucleus (Bregma -1.82mm, -2.06mm and -2.30mm), two levels of substantia nigra (Bregma -3.08mm and -3.64mm) were selected to cover the extent of the regions depicted in the atlas.³⁶ Stitching and maximum intensity projection images were generated using custom-made macros in Fiji. Automatic nuclei and synaptic spot detection was carried out in Imaris (v9.1.2. Oxford Instruments, Bitplane). Automatic spot detection was visually validated on every section for all experiments. Neurons were detected using TrackMate⁵⁹ assisted by manual curation. The coordinates of detected markers were subsequently transformed into the Allen Brain Atlas Common Coordinate Framework as previously described.⁶⁰ Coordinates of Bregma in Allen CCF were set at AP, 5400; ML, 5700; DV 0^{60,61} and were divided by 1000 so that the coordinates in Allen CCF were converted to coordinates in mm⁶⁰ to fit with a widely-used brain atlas with a numerical coordinate frame.³⁶

Extracted coordinates were used to plot the distribution of labeled neurons using custom-built scripts in Python 3.7. 1D density plots were generated using 1D-kernel density estimate (1D-KDE) on antero-posterior, dorso-ventral or medio-lateral axis. The laterality index in [Figure S2F](#) were estimated by calculating the medio-lateral distribution of the synaptic puncta using bins of 30 μm and obtaining a weighted mean of the centers of the bins, weighted with the proportion of synapses in that bin. 2D density plots were generated using 2D-kernel density estimate (2D-KDE), plotting 5 or 7 density lines covering the space of 10-100% or 30-100% of highest density using Scipy, a Python library for scientific computing. To perform spatial correlation analysis, the density of synapses (binning into 100x100 pixels for each injection site) from one or multiple sections calculated using 2D-KDE was vectorized, and a correlogram was formed by calculating pairwise cosine similarity (scikit-learn library) between any two injection sites. Hierarchical clustering was performed using the clustering package in Scipy with the Ward variance minimization algorithm in the linkage function using the cosine distances calculated above. For the 3D density of postsynaptically labelled neurons shown in [Video S3](#), the

converted cell coordinates were plotted with a custom written code based on the Points function and the PointsDensity function, with a cutoff of 10%, in Brainrender⁶² and the color gradient and transparency of the color reflects the density of the distribution of the labelled neurons.

MouseLight database analysis

MouseLight is a database from the Janelia Research Campus in which single neurons are reconstructed and registered to the Allen CCF.⁴ To make use of this resources, we turned to MouseLight NeuronBrowser (<http://ml-neuronbrowser.janelia.org/>) and searched for neurons with the following criteria: soma in the cerebral cortex and axon in the medulla, which yielded a total of 39 neurons. We then looked for the number of axon terminals in the medulla following an established method.⁶³ Those with more than 5 axon terminals in medulla were further analyzed, resulting in a total of 17 neurons. To map the position of the soma in the cortex, the coordinates of the soma of each neuron in Allen CCF were subtracted by the coordinates of Bregma in Allen CCF (AP, 5400; ML, 5700; DV 0)⁶¹ and were divided by 1000 so that the coordinates in Allen CCF were converted to coordinates in mm⁶⁰ to fit with a widely-used brain atlas with a numerical coordinate frame.³⁶ For neurons whose soma locations are at the left hemisphere, the ML coordinates were mirrored. From the 17 chosen neurons, 13 resided in the anterior cortex (AP coordinates more than 1mm from bregma, Figure 1C), which were included for further analysis. Among these 13 neurons, 7 neurons resided in the MAC region (ML coordinates less than 1.5mm from midline, Figure 1D; AA0180, AA0012, AA0250, AA0788, AA0179, AA0576, AA0726) and 6 neurons resided in the LAC region (ML coordinates more than 1.5mm from midline, Figure 1D; AA1543, AA0133, AA0134, AA0169, AA1043, AA0956). We also obtained the converted coordinates of axon terminals contralateral to the soma from each of these neurons. We plotted the distribution of axon terminals from each neuron along the AP axis in the medulla with the 1D-kernel density estimation. 2D density plots of the distribution of the axon terminals were generated using a 2D-kernel density estimate plotting 5 density lines covering the space of 10-100% of highest density equally using Scipy. Here, the mediolateral and dorsoventral coordinates of all the terminals was used throughout the anteroposterior extent of the medulla.

Behavioral analysis of forelimb movements

For analysis of the behavioral effects upon silencing of cortical domains compared to control conditions, we used deep neural network based markerless pose estimation using DeepLabCut³⁸ coupled with high-speed videography of the bottom view of the mouse using Basler Ace2 cameras controlled using Bonsai.⁶⁴ We used a DeepLabCut model trained using 1100 frames of different videos of mice from the bottom view over behavioral experiments in the lab, with at least 15 frames of each video corresponding to all the different sessions of each mouse in the silencing experiment. The training frames were annotated with the following body parts: nose, head base, hand, wrist, body center, hindlimb ball, hindlimb heel, genitalia and tail base.

All trials of reaching and handling were annotated manually from the behavioral videos. In case of MAC silencing, all mice (n=9) were unable to substantially extend their forelimbs. We therefore annotated attempts where they arrived at the slit and tried to move their forelimb towards the pellet with an apparent desire to reach the pellet. Upon LAC silencing, mice often resorted to eating of the food pellet without forelimb manipulation and these trials were annotated separately and quantified in Figure 5E. When mice did handle the food pellet with their forelimbs, they displayed a tendency to drop the pellet, and these trials were annotated and quantified separately in Figure 5E (right). During food handling, we also annotated the number of regrips in each handling bout quantified in Figure 5F. For the analysis with DLC, the reaching and handling trials were filtered such that trials in which the reaching forelimb hand was not tracked reliably with a confidence level (p) below 0.4 for over 5 frames overall in the trial were excluded and at least 10 trials of each were included for each session. For the others, in case of p falling below the threshold of 0.4, we linearly interpolated the trajectories. For handling, we also annotated the number of regrips during food manipulation.

For the analysis of reaching trajectories as shown in Figure 5D, we plotted the trajectories for an example mouse. The trajectory was smoothed with a Savitzky-Golay filter with a window size of 5 frames (50ms) and polynomial order of 2. To obtain the average trajectory, we normalized the time from the start of the reach to the time of maximal extension between 0 and 1 and discretized it into 10 equal bins. The individual trials shown for the example mice have all timepoints displayed, with each point representing 1 frame (10ms) apart and color-coded with the normalized time. Three of the mice (3/9) were right handed and their reaching trajectories were flipped to make their trajectories comparable to the left handed mice. The trajectory obtained from each mouse was averaged and is displayed in Figure 5D (lower right). The maximum extension shown in Figure 5C was the maximum extension of the limb relative to the slit in the entire session. The reaching velocity was calculated using the differential of the trajectory in the two planes and the magnitude of the velocity was median filtered and estimated as the speed of the forelimb in Figure 5C. For handling, we again smoothed the trajectories of both forelimb hands using a Savitzky-Golay filter as detailed above. The trajectories were then rotated such that the axis along the tailbase and midpoint of the forelimb hands at the start of the handling bout was vertically aligned. To study primarily the movement of the distal limbs, the coordinates were shifted such that the midpoint between the limbs was always at the origin at all timepoints. In Figure 5G, the trajectories of 7 handling trials are displayed for each condition, colored by normalized time. We quantified the movement of the distal limbs as the standard deviation (s.d.) of the forelimb hands' coordinates obtained above averaged for the two hands over all trials, for each mouse across each experimental condition. To account for differences between mice, the s.d. of the hands during handling was calculated for each mouse across three conditions. To normalize s.d. across mice, we divided each of the values by the maximum s.d. for each mouse. The average normalized s.d. are shown in Figure 5F.

Analysis of electrophysiological recordings

For analysis of extracellular electrophysiology recordings using Cambridge Neurotech probes, recordings were sorted using Kilosort2⁶⁶ to obtain isolated single units. The units were then manually curated using Phy 2 (<https://github.com/cortex-lab/phy>) to obtain single units which were used for subsequent analyses. Briefly, we used typical heuristics to identify well isolated single units, using unit waveforms and spiking amplitudes, autocorrelogram for identification of a clear refractory period and considering merges and splits using Phy 2 as described in its documentation. To confirm correct probe placement and to locate recordings sites, a small current (3s at 200 mA) was delivered near the tip of the Cambridge NeuroTech probe using an electrical stimulator (WPI Inc., Stimulus isolator A360).

For Neuropixels 1.0 probes, we used the SpikeGLX system to record the electrophysiology signal in synchrony with the laser pulses and camera timestamps collected using the National Instruments PXIe-6341 multifunction IO module coupled with the BNC-2110 breakout box using the National Instruments PXIe/PCIe-8281 controller module. The data was processed using the ecephys spike sorting modules for SpikeGLX (https://github.com/jenniferColonell/ecephys_spike_sorting). Briefly, data collected from SpikeGLX was first processed with the CatGT module to apply demultiplexing corrections and for highpass filtering the data. Additionally, the edges of the synchronization pulses from the IMEC base station on which the Neuropixels data was recorded, the camera exposure pulses and laser pulses were extracted. Subsequently, using the Kilosort helper module, channels with firing rate below 0.05 Hz were excluded as noisy channels and the channel map for the spatial location of the remaining channels was constructed using the metadata from the recordings. We used Bank 0 on the Neuropixels 1.0 to record from the ventral most 384 channels on the probe. Subsequently, Kilosort3 was run on the data. Following the sorting, TPrime module helped synchronize all the datastreams precisely with the IMEC base station recording used as the reference time stream using the synchronization pulse recorded on both the multifunctional IO device and the IMEC base station. To identify the units in the LatRM, we registered the probe tract identified using the Dil, which was used to mark the Neuropixels probes, to the Allen CCF (https://github.com/petersaj/AP_histology). Using the “ephys alignment tool” from the International Brain Laboratory (<https://github.com/int-brain-lab/iblapps/wiki>), we aligned the electrophysiological features from the data with the anatomical landmarks to obtain the precise trajectory of the probe. Subsequently, the units on the channels in the LatRM were identified and used for further analysis. We then performed the manual curation of the output of Kilosort3 in Phy 2 to obtain isolated single units as stated above.

We recorded a total of 726 single units across 13 mice. To determine latRM neurons that modulated their firing in response to different phases of the forelimb reaching and handling task, we calculated Modulation Indices (MIs) for the pre-reaching, reaching, retraction and handling phases. The firing rate was binned into bins of 5ms for subsequent analysis. Briefly, for these behaviors, we calculated the MIs for each trial of the behavior for each neuron as the average firing rate in the behavior window in that trial above the baseline. The distribution of MIs obtained was compared to the distribution of MIs obtained for the same neuron from 1000 random timepoints in a time window equal to the average length of the behavior phase in question using a Mann Whitney U-test. A neuron was classified as positively modulated to a behavioral phase if it had a p-value < 0.01 for this comparison and the average of the MI over all the trials of the behavior was greater than 3. It was classified as negatively modulated at a p-value < 0.01 and MI value < -3. The validity of this approach can be seen on the heatmap showing the activity of all neurons identified as positively (Figure S6) or negatively (Figure S7) modulated to one of the behavioral phases. Using the same method, we defined neurons modulated to application of laser light to the cortex as those that significantly changed their firing rate (p-value < 0.001 and MI > 3) in the first 20ms following the onset of the laser that stimulated the cortical neurons (Figures 6C and S5D). The time windows to calculate the baseline for each trial for each behavioral phase or laser simulation are defined as following: -0.75s to -0.5s for pre-reach and reach (0s as reach onset); -1s to -0.75s for retract (0s as retract onset); -1.25s to -1s for handle (0s as handle onset); -0.75s to -0.25s for laser (0s as laser onset). This pipeline is briefly summarized in Figure S5A. The overall baseline firing rate of each neuron displayed in the activity heatmaps was determined as the average firing rate over the recording session.

In the heatmaps used to display the average activity of the single neurons in Figures 6D and S5E, we first baseline subtracted the activity of the neuron and then normalized the baseline subtracted activity between 0 and 1. For the average activity of the population of neurons modulated from the MAC or the LAC aligned to reach or handle start, we first normalized the activity of all neurons and subtracted the baseline activity of each neuron estimated as the average activity in the time window of -4s to -3s from the onset of the behavior. The normalized average population activity is displayed in Figure 6D.

Statistics

Significance levels indicated are as follows: * $p < 0.05$, ** $p < 0.01$, *** $p < 0.001$. All values reported in the text and figures represent mean \pm SEM. All statistical analyses were performed using Scipy, statsmodels, and Pingouin packages in Python 3.7. Shapiro-Wilk normality test was applied to check if the data set was normally distributed. Non-normally distributed data were subsequently compared with non-parametric tests. The following statistical tests were used to assess significance when indicated. To compare the cortical depth of the latRM and spinal cord projecting neurons, we used Wilcoxon rank-sum test (MAC, $p = 0.0495$; CFA, $p = 0.0495$). To compare the number of synapses from different cortical sites in Figures 2 and S2, we used one-way ANOVA followed by the Tukey HSD test. For rostral medulla levels, $F_{(4, 25)} = 26.04$, $p < 0.001$, pairwise comparison as follows: MAC vs. LAC, $p = 0.2149$; MAC vs. CFA, $p < 0.001$; MAC vs. InsC, $p < 0.001$; MAC vs. Pos, $p < 0.001$; LAC vs. CFA, $p = 0.0349$; LAC vs. InsC, $p = 0.0376$; LAC vs. Pos, $p < 0.001$; CFA vs. InsC, $p = 0.9$; CFA vs. Pos, $p < 0.001$; InsC vs. Pos, $p = 0.0444$. For intermediate medulla levels, $F_{(4, 25)} = 11.33$, $p < 0.001$, pairwise comparison as follows: MAC vs. LAC, $p = 0.9$; MAC vs. CFA, $p = 0.018$; MAC vs. InsC, $p = 0.0244$; MAC vs. Pos,

$p < 0.001$; LAC vs. CFA, $p = 0.0344$; LAC vs. InsC, $p = 0.042$; LAC vs. Pos, $p < 0.001$; CFA vs. InsC, $p = 0.9$; CFA vs. Pos, $p = 0.1054$; InsC vs. Pos, $p = 0.6736$. For caudal medulla levels, $F_{(4, 25)} = 15.28$, $p < 0.001$, pairwise comparison as follows: MAC vs. LAC, $p = 0.2838$; MAC vs. CFA, $p < 0.001$; MAC vs. InsC, $p < 0.001$; MAC vs. Pos, $p < 0.001$; LAC vs. CFA, $p = 0.0424$; LAC vs. InsC, $p = 0.0198$; LAC vs. Pos, $p < 0.001$; CFA vs. InsC, $p = 0.7757$; CFA vs. Pos, $p = 0.1813$; InsC vs. Pos, $p = 0.9$. To compare the peak of synaptic distribution along the dorso-ventral axis in [Figure 3](#), we used two-way ANOVA followed by the Tukey HSD test. For D-V peak across medullary levels, $F_{(2, 60)} = 1.359$, $p = 0.265$; For D-V peak across cortical regions, $F_{(3, 60)} = 48.779$, $p < 0.001$, pairwise comparison as follows: MAC vs. LAC, $p < 0.001$; MAC vs. CFA, $p = 0.00896$; MAC vs. InsC, $p < 0.001$; LAC vs. CFA, $p < 0.001$; LAC vs. InsC, $p < 0.001$; CFA vs. InsC, $p < 0.001$. To compare the behavioral performance in [Figure 5](#), we used two-way ANOVA followed by the Tukey HSD test, except for the reach speed which was compared with the paired t-test. For the number of reaches per minute, $F_{(2, 16)} = 13.116$, $p < 0.001$, pairwise comparison as follows: MAC vs. LAC, $p < 0.001$; MAC vs. Con, $p = 0.0025$; LAC vs. Con, $p = 0.2107$. For maximum extension, $F_{(2, 16)} = 47.071$, $p < 0.001$, pairwise comparison as follows: MAC vs. LAC, $p < 0.001$; MAC vs. Con, $p < 0.001$; LAC vs. Con, $p = 0.026$. For reach speed, $p = 0.676$. For percentage of eating without forelimb, $F_{(2, 16)} = 72.166$, $p < 0.001$, pairwise comparison as follows: MAC vs. LAC, $p < 0.001$; MAC vs. Con, $p = 0.3466$; LAC vs. Con, $p < 0.001$. For percentage of pellet drop during eating, $F_{(2, 14)} = 40.311$, $p < 0.001$, pairwise comparison as follows: MAC vs. LAC, $p < 0.001$; MAC vs. Con, $p = 0.966$; LAC vs. Con, $p < 0.001$. For the number of regrips per second, $F_{(2, 14)} = 15.72$, $p < 0.001$, pairwise comparison as follows: MAC vs. LAC, $p = 0.00898$; MAC vs. Con, $p = 0.7747$; LAC vs. Con, $p < 0.001$. For normalized SD of FLs during handling, $F_{(2, 14)} = 8.93$, $p = 0.00316$, pairwise comparison as follows: MAC vs. LAC, $p = 0.0457$; MAC vs. Con, $p = 0.0841$; LAC vs. Con, $p < 0.001$. To compare the averaged firing rate between modulated neurons in [Figure 6](#), we used the Wilcoxon signed rank test. For firing rate aligned to reach onset, the task window is defined by -0.5 to 0.5s from reach onset, MAC vs. LAC, $p < 0.001$. For firing rate aligned to handle onset, the task window is defined by handle onset to 1s, MAC vs. LAC, $p < 0.001$.

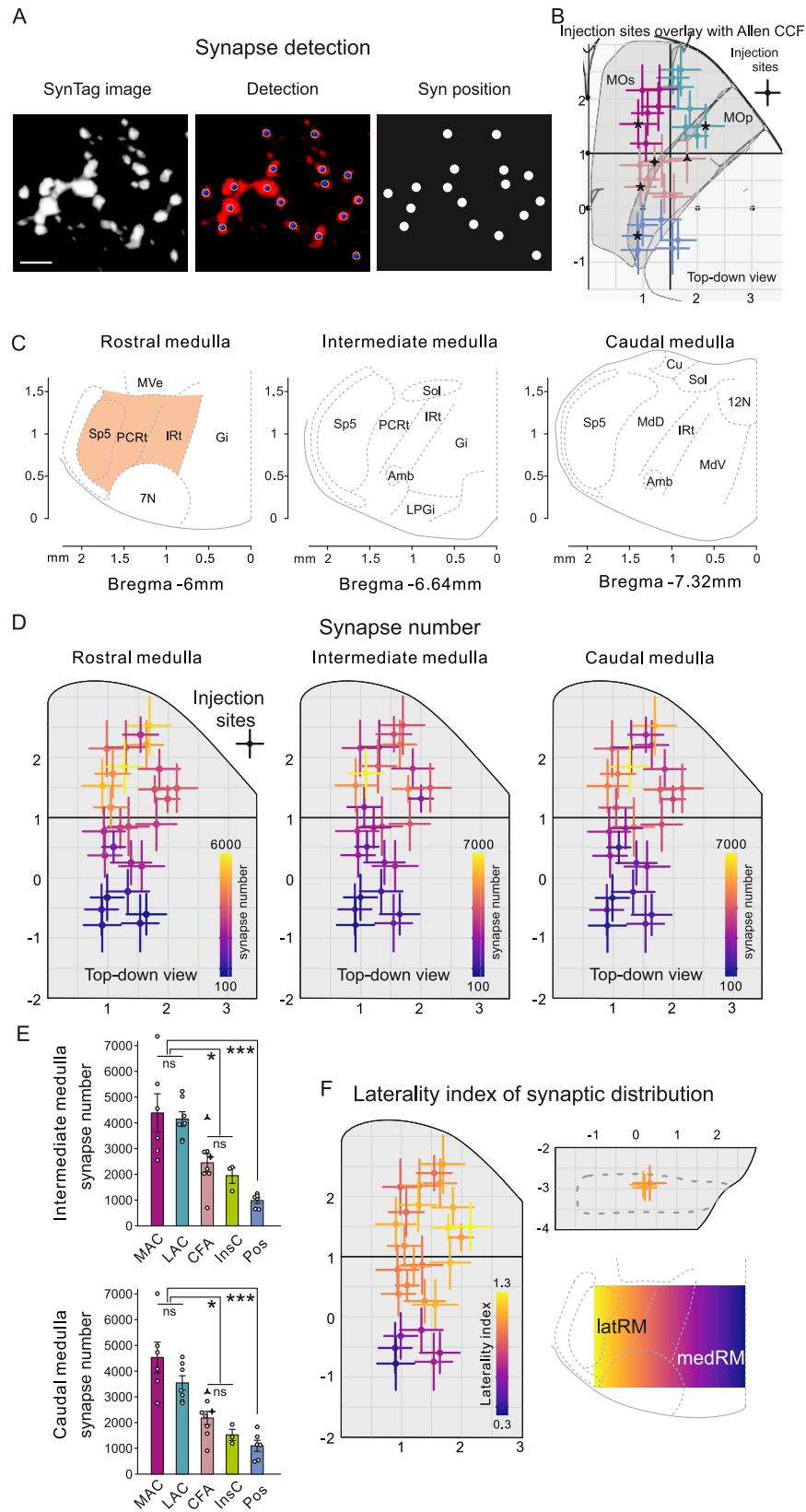


Figure S2. Anterior cortex targets lateral rostral medulla, related to Figure 2

(A) Representative example of synaptic terminal analysis with high-resolution imaging and Imaris spot detection. Scale bars, 10 μ m.

(B) Scheme showing cortical injection sites from Figure 2B overlaid with the atlas of Allen CCF for comparative purposes.

(C) Schematic showing the three medullary levels analyzed in this study as rostral, intermediate and caudal medulla, respectively according to a well-known atlas.³⁶ Color-coded region is the area here referred to as lateral rostral medulla (latRM). Sp5, spinal trigeminal nucleus; PCRt, parvicellular reticular nucleus; IRt, intermediate reticular nucleus; 7N, facial motor nucleus; Gi, gigantocellular reticular nucleus; MVe, medial vestibular nucleus; Amb, ambiguus nucleus; Sol, solitary nucleus; LPGi, lateral paragigantocellular reticular nucleus; 12N, hypoglossal motor nucleus; MdV, medullary reticular nucleus, ventral part; MdD, medullary reticular nucleus, dorsal part; Cu, cuneate nucleus.

(D) Synapse numbers in rostral, intermediate, and caudal medulla from cortical injection sites shown in Figure 2B.

(E) Number of synapses at corresponding medullary levels from cortical sites grouped as shown in Figure 2B (mean \pm SEM). Triangle and diamond shapes indicate injection sites marked in Figure 2B. MAC, n = 6; LAC, n = 7; CFA, n = 8; lnsC, n = 3; Pos, n = 6. *p < 0.05; ***p < 0.001; ns, not significant.

(F) Laterality indices of the synaptic distributions from individual injection sites in the cortex and summary scheme (bottom right) depicting the high density of cortical synapses in the lateral (latRM) as opposed to the medial (medRM) rostral medulla.

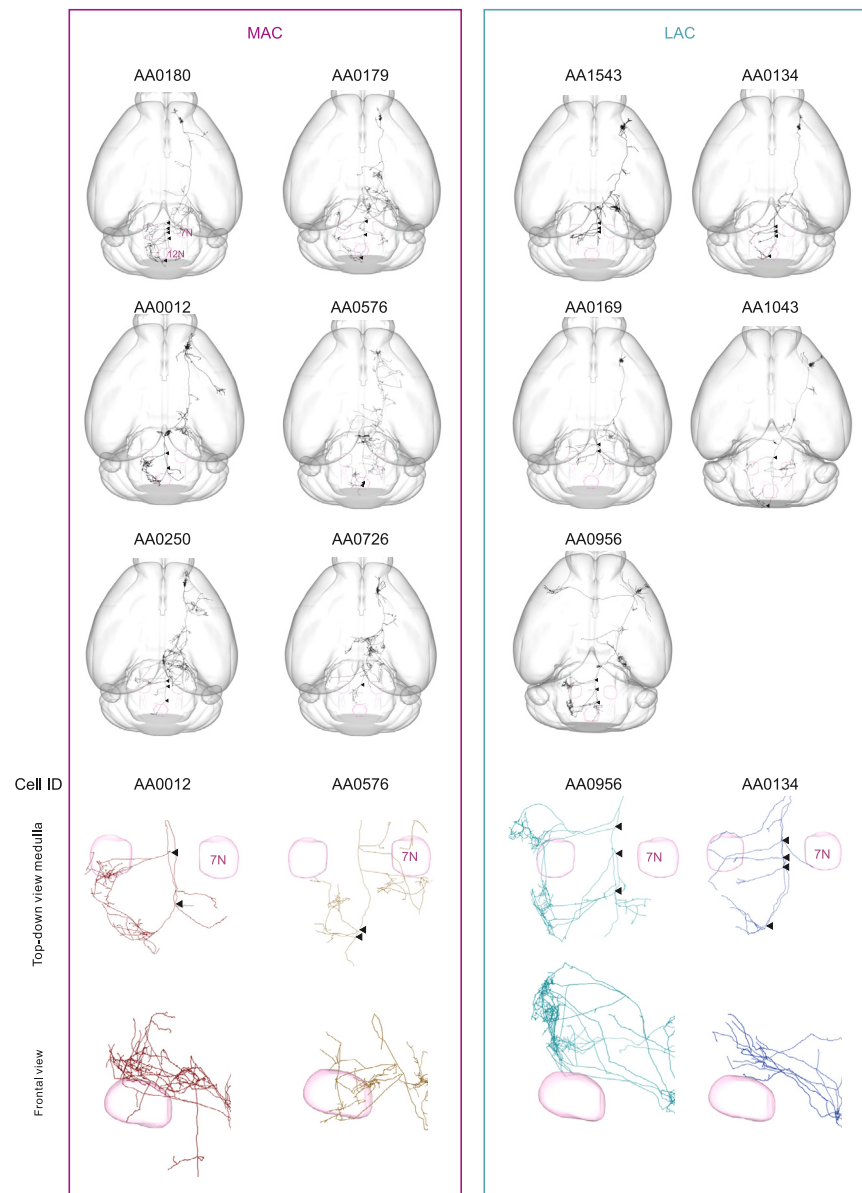


Figure S3. Single MAC and LAC neurons from MouseLight database, related to Figure 4

Top: top-down view of overall axonal processes from single MAC (magenta) and LAC (cyan) neurons. Bottom: top-down (upper) and frontal view (lower) zoom-in views of axonal processes in the medulla from single cortical neurons at higher magnification. Triangles denote axonal collaterals exiting from the parent main axon.

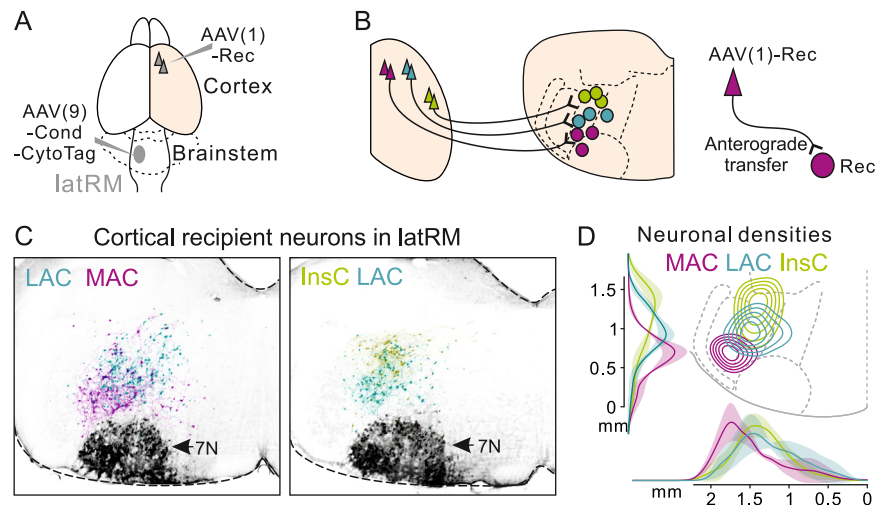


Figure S4. Cortico-medullary synaptic organization extends into postsynaptic medulla, related to Figure 6

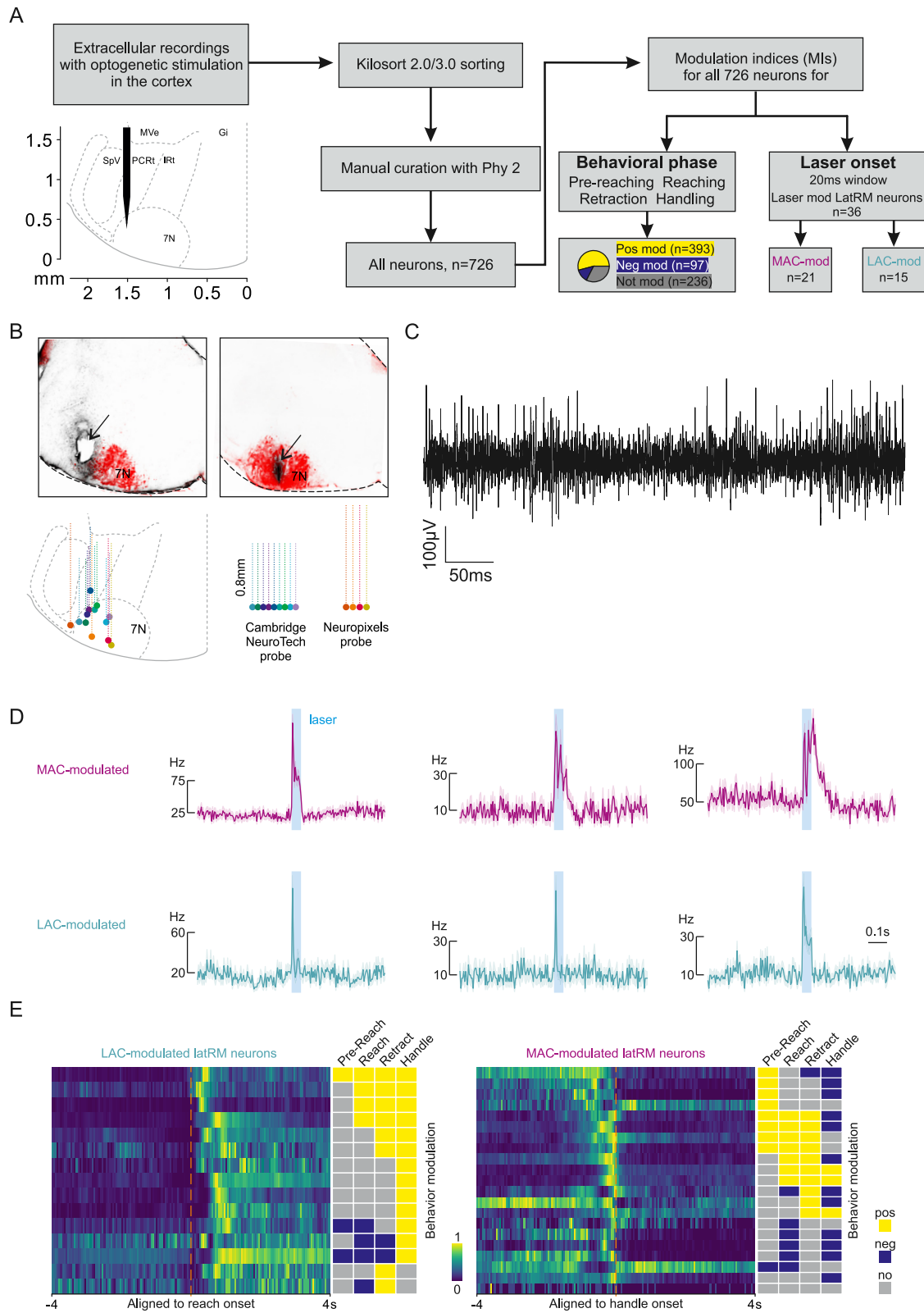
(A) Strategy for labeling medulla neurons with cortical input from different cortical regions.

(B) Scheme showing the strategy of using AAV(1) virus to label postsynaptic neurons through anterograde transfer of recombinase (Rec) expressing virus.

(C) Representative coronal rostral medulla sections from two mice showing the infected postsynaptic neurons receiving input from MAC, LAC, and InsC.

(D) Averaged 2D, dorso-ventral and medio-lateral density distribution of postsynaptic neurons in the rostral medulla receiving input from MAC (n = 3), LAC (n = 4), and InsC (n = 3).

See also [Video S3](#).



(legend on next page)

Figure S5. Analysis of electrophysiology data, related to Figure 6

(A) Scheme of the pipeline for extracellular electrophysiology recording and analysis.

(B) Top: representative latRM sections from mouse undergoing single-unit recordings with Cambridge NeuroTech probe (left) or Neuropixels probes (right). The end point of the silicon probe trajectory is either visualized directly (left) or from Dil painted on probes (right). Sections are counterstained for ChAT to visualize 7N neurons (red). Bottom: Reconstruction of probe placements at the rostral medulla level. Dots denote the tips of the probe while the dashed lines show the estimated extension of the probes. Each color corresponds to one mouse analyzed for data shown in Figure 6.

(C) Example of a raw unsorted extracellular voltage trace.

(D) Example latRM neurons showing the effect of cortical MAC (magenta) or LAC (cyan) stimulation.

(E) Heatmaps for baseline subtracted and normalized firing of single neurons for the LAC-modulated (left, aligned to reach onset) and MAC-modulated (right, aligned to handle onset) populations (data from Figure 6D).

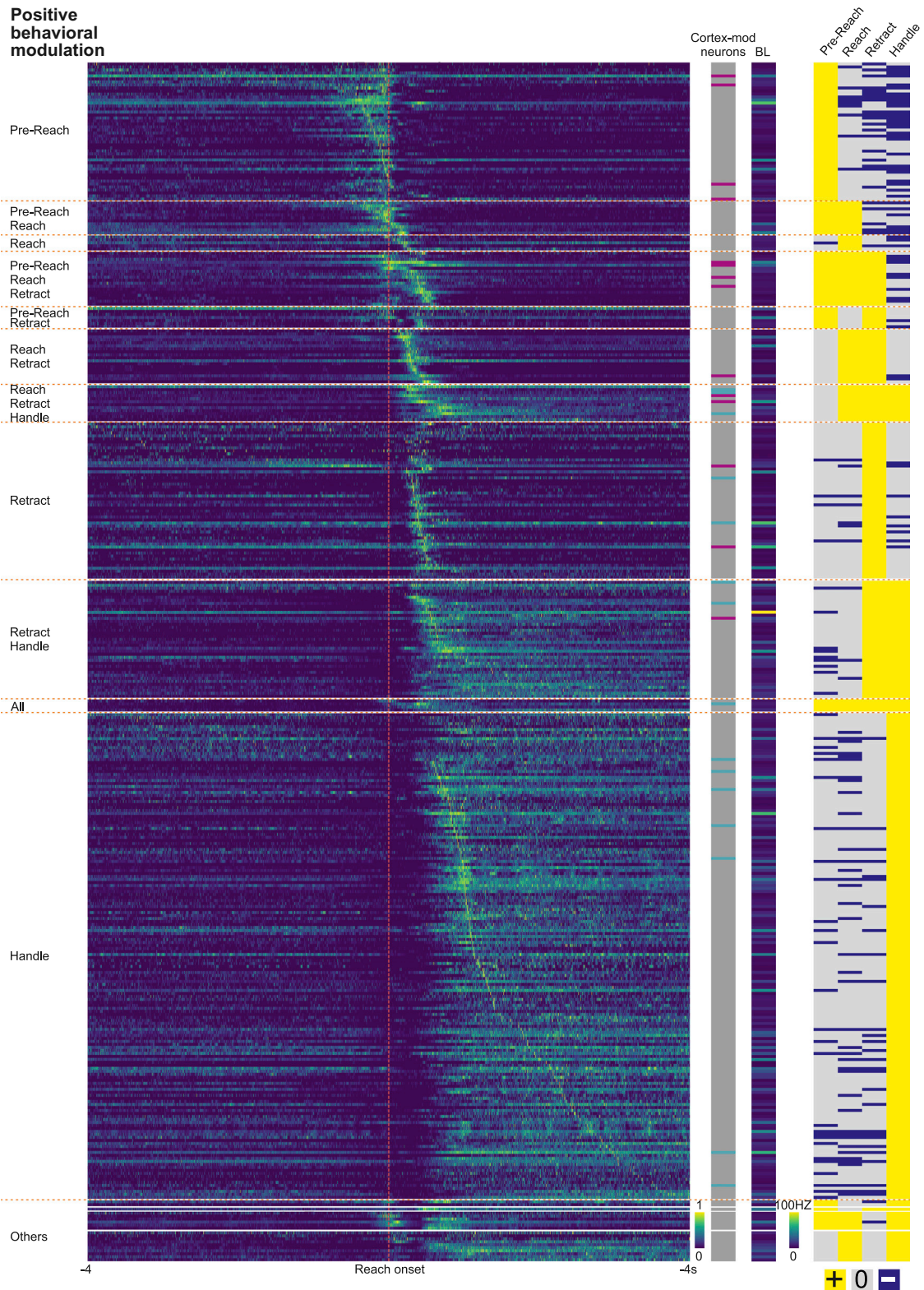


Figure S6. Positively modulated latRM neurons in reaching and handling tasks, related to Figure 6

Heatmap showing the normalized firing rate of all single neurons in latRM positively modulated in reaching and handling ($n = 393$). On the right, neuron identity is indicated in magenta (MAC-modulated), cyan (LAC-modulated), or gray (not modulated) depending on modulation properties, next to its baseline firing rate (BL) and the modulation in different behavioral phases (yellow: positive modulation; blue: negative modulation; gray: no modulation).

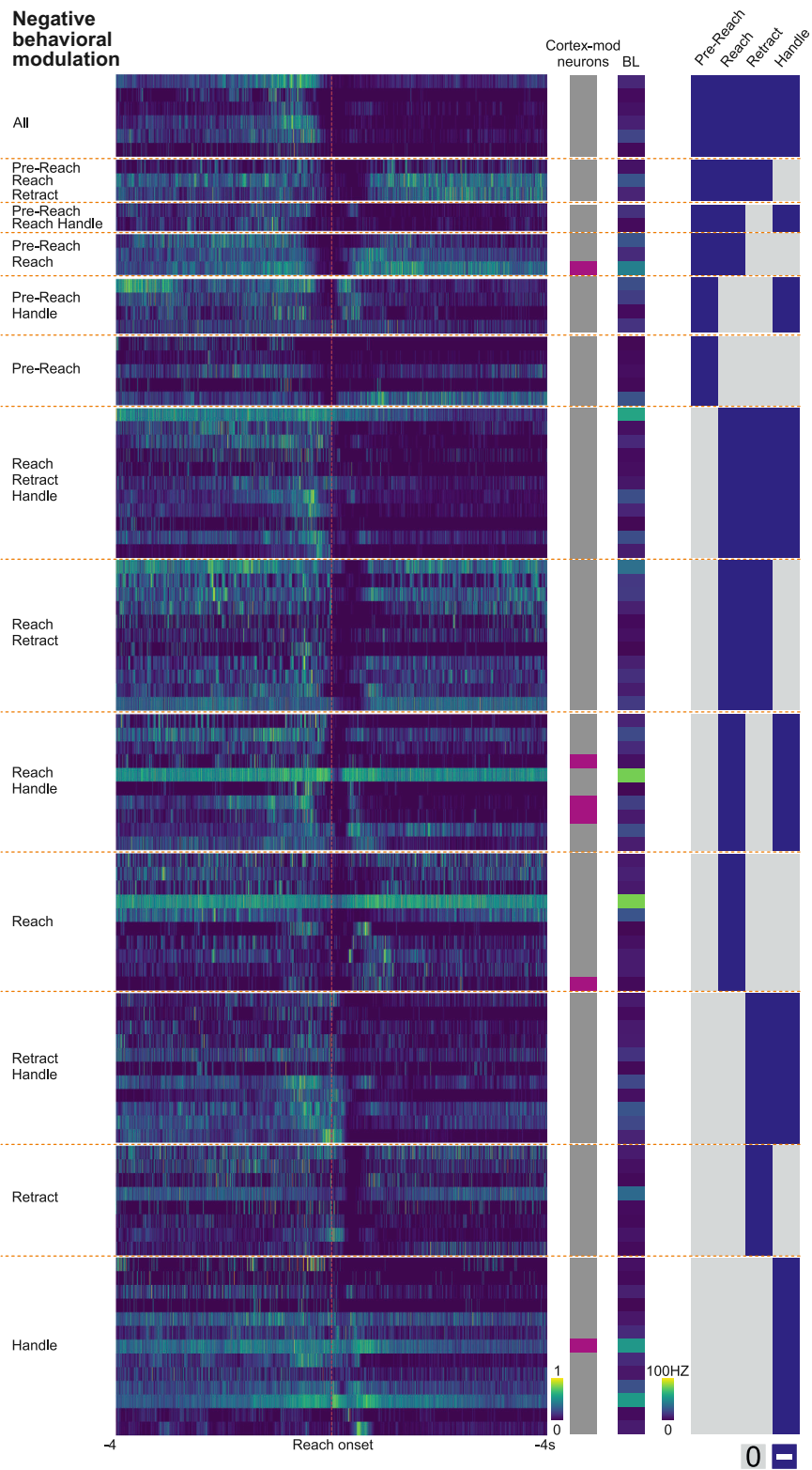


Figure S7. Negatively modulated latRM neurons in reaching and handling tasks, related to Figure 6

Heatmap showing the normalized firing rate of all single neurons in latRM negatively modulated in reaching and handling ($n = 97$). On the right, neuron identity is indicated in magenta (MAC-modulated) or gray (not modulated) depending on modulation properties, next to its baseline firing rate (BL) and the modulation in different behavioral phases (blue: negative modulation; gray: no modulation). Note that no LAC-modulated neurons were found in this category.

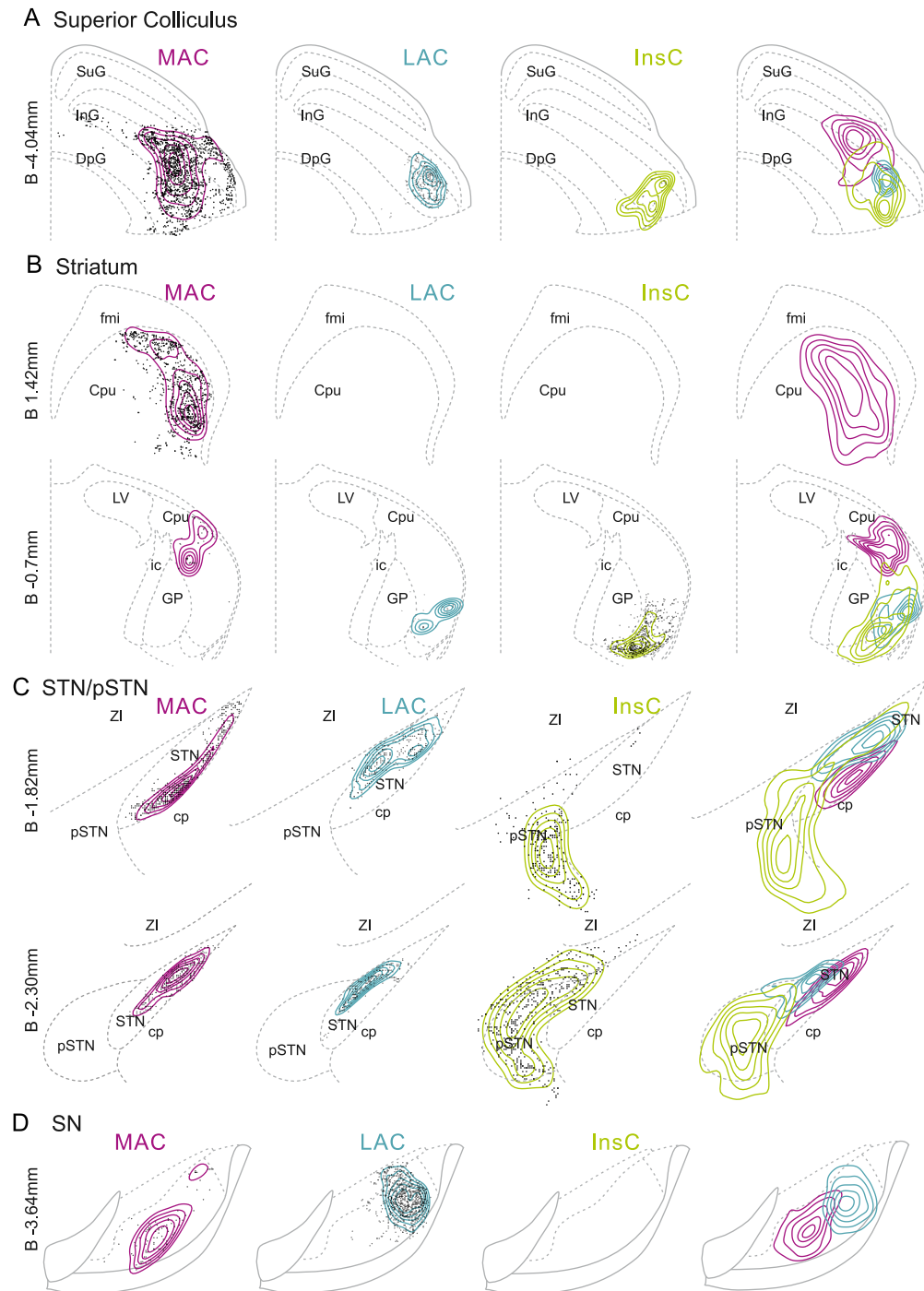


Figure S8. Differences in synaptic targeting of cortico-medulla neurons extends to other subcortical structures, related to Figure 7

Example 2D reconstruction of synaptic puncta and density distributions in superior colliculus (A), striatum (B), STN/pSTN (C), and substantia nigra (D) at denoted levels from 3 mice with labeled cortico-medullary neurons in MAC, LAC and InsC. Right: 2D reconstruction of averaged synaptic density distribution from MAC, LAC, and InsC overlaid.